Early-Time Dynamics of the Photoexcited Hydrated Electron

4 AUTHORS, INCLUDING:

Douwe A. Wiersma
University of Groningen
203 PUBLICATIONS   7,235 CITATIONS

Early-Time Dynamics of the Photoexcited Hydrated Electron

Andrius Baltuška, Michel F. Emde, Maxim S. Pshenichnikov, and Douwe A. Wiersma*

Ultrafast Laser and Spectroscopy Laboratory, Department of Chemistry, University of Groningen, Nijenborgh 4, 9747 AG Groningen, The Netherlands

Received: July 19, 1999; In Final Form: October 1, 1999

Employing photon echo techniques, we investigate the early relaxation dynamics of the equilibrated hydrated electron within the first 200 fs upon photoexcitation. The use of 5-fs laser pulses provided unprecedented temporal resolution of our measurements. We show that even for extremely short pulse durations the signals obtained in photon echo spectroscopy, can be described in the conventional way, provided care is taken of the spectral filtering effect and experimental beam arrangement. We next conclude that the absorption spectrum of the hydrated electrons is primarily homogeneously broadened. The comparison of two pulse photon echo experiments on pure water and on hydrated electrons allows us to measure the pure dephasing time of ~1.6 fs. The line shape of the absorption spectrum is described excellently by an extended Lorentzian contour with a spectral width fully determined by the pure dephasing time. From the polarization-dependent transient grating experiments we establish that the polarization anisotropy of the hydrated electron falls to the zero value within 5 fs after initial excitation. A prominent role of a non-Condon effect due to strong coupling of the electron to neighboring water molecules is suggested. Based on the observed isotopic effect we concluded that the initial relaxation dynamics are determined by the inertial response of the water molecules which is librational in its origin. The microscopic picture of the early dynamics of the hydrated electron based on the experimental results is presented. Finally, we develop a theoretical model based on wave packet dynamics, which is capable of capturing the subtle features of the experimental data.

1. Introduction

Upon injection into a fluid, an electron can be captured in a potential energy well formed by neighboring molecules of the liquid. The first observation of such an electron, known nowadays as the solvated electron, dates back to 1864, when Weyl reported a blue color of solutions of metals in ammonia.[1] However, it took more than half a century until Kraus[2] suggested that the blue color was caused by bound species: electrons trapped among the ammonia molecules. The solvated electron has been the subject of numerous investigations ever since. In the sixties the electron solvated in water, called the hydrated electron*,* was discovered through the observation of the extraordinarily broad absorption spectrum spanning from 500 to 1000 nm that appeared upon injection of electrons.[3,4]

The vast interest in the hydrated electron from both theoretical and experimental points of view is by no means accidental. The hydrated electron is a transient species in charge-transfer reactions in biology, nonsilicon solar-cell technology,[5–8] and chemistry. Important examples are photosynthesis,[9] charge transport through biomembranes,[10] and long-distance charge transport in nerves.[11] The hydrated electron is also a key intermediate in radiation chemistry[3] and electrochemistry.[5–8] Next to this, the hydrated electron is a perfect test-ground for various theories of complex quantum-mechanical systems. The three-dimensional confinement of the single electron by the surrounding water molecules gives rise to discrete quantum states. This closely resembles a quantum dot,[12] an entity that has raised considerable attention in recent years as a model system for atoms[13–15] and molecules,[16] and holds a great

promise for use in optical devices.[17] However, the important difference between the quantum dot and the hydrated electron is that in the former case the potential giving rise to the confinement is static, whereas in the latter case it changes rapidly in time due to dynamical fluctuations of the liquid surrounding.

Numerous computational studies have been performed to investigate the quantum-mechanical status of the hydrated electron and the microscopic structure of its surroundings. It became clear that the first shell of water around the electron is composed of approximately six molecules with their OH bonds oriented toward the electron.[18,19] A similar result was also found in electron-spin–echo measurement on the electron solvated in glassy water.[20,21] When the molecular dynamics simulations matured, they succeeded in reproducing the general features of the absorption band shape, such as its breadth and asymmetry,[18,22–25] although the transition energies were somewhat overestimated. After being shifted toward lower frequencies, the simulated spectra closely resembled the experimental data. According to the extensive computational modeling performed by the group of Rossky,[18,23,24] the absorption spectrum of solvated electrons is primarily caused by a strongly allowed transition from a roughly spherical localized *s*-like ground state to a triple of *p*-like states that are also bound and localized. The existence of the *s*-state indicates that on average the potential energy well created by the molecules surrounding the electron, is close to spherical. However, because of the asymmetries caused by the dynamical nature of liquid water, the potential energy surface does not have a perfect spherical shape, which results in three nondegenerate *p*-states.

The question about homogeneous vs inhomogeneous broadening in the optical absorption spectrum of the excess electron in water and other fluids, as well as the explanation of its

---

* Corresponding author fax, +31-50-3634441; phone, +31-50-3634615; e-mail, D.A.Wiersma@chem.rug.nl

asymmetry and extraordinary spectral width, has remained a standing problem for over three decades. Numerous attempts have been made to fit the experimental data by various line shapes[26-30] and superposition of lines.[31-33] In the computer simulations,[23] by imposing an ordering of the *p*-states according to their energy, the resulting absorption contour was decomposed into a superposition of the contributions from separate $s-p$ transitions. Each of the obtained three bands is claimed to be substantially inhomogeneously broadened by different structures of the solvent surroundings. The energy splitting between two adjacent $s-p$ transitions found in these simulations is ∼0.4 eV, which nearly constitutes the width of the bands associated with each separate transition.

The dynamical behavior of the hydrated electron, i.e., the energy relaxation after an instantaneous $s{\rightarrow}p$ excitation, has been thoroughly modeled as well.[18,19,25,34-41] All computer simulations predict that the solvation dynamics are essentially bimodal. The initial decay is responsible for ∼50% of the total energy relaxation and occurs at a 10−25 fs time scale which is followed by a slower 130−250 fs decay. It is generally agreed that the latter time scale results from the diffusional motion of water molecules into and out of the first solvation shell.

However, the microscopic nature of the fast initial decay is still under considerable debate. By comparing the frequencies from the power spectrum of the correlation function of the $s-p$ energy gap with the Raman spectrum of water, Staib et al.[25] concluded that the accelerated decay was determined by coupling to hindered rotations of water molecules, generally called *librations*. Based on the dependence of the most rapid time scale in ordinary and deuterated water, Barnett et al. found that the initial dynamics of the hydrated electron is caused by *free* rotational diffusion of water molecules.[34] Conversely, Berg[41] and the group of Rossky[36-38] revealed no isotope effect in the first 25 fs of the solvation dynamics of the hydrated electron. They accordingly inferred that the origin of the initial dynamics is translational. Park et al. concluded that the motions of the water molecules in the first solvation shell of the hydrated electron are dominantly rotational through repulsion of hydrogen-bonded hydrogen atoms and attraction of dangling hydrogen atoms.[19]

The past decade has witnessed numerous studies of the hydrated electron with an ∼200-fs time resolution.[33,42-50] The femtosecond time-resolved studies of hydrated electrons were pioneered by Migus et al.[42] The electrons were generated by multiphoton ionization of neat water and studied by transient absorption of a super-continuum probe. Later, similar experiments were carried out by several groups evidencing the importance of geminate recombination and pump−probe cross-phase modulation in the recorded transients.[33,43,44,47-50]

In another approach, the already-equilibrated hydrated electron is excited from the ground *s*-state to the *p*-state using a short pulse, and the resulting solvation dynamics is probed as a function of time with another, delayed, pulse. Following this route, the group of Barbara found decays of ∼300 fs and ∼1.1 ps in a pump−probe experiment.[51] The results were explained using a three-state model, where the fastest decay is caused by the relaxation down to the ground state, giving rise to a not yet-equilibrated "hot" ground state. Recently Assel et al. refined this model by including excited-state solvation that took place before relaxation back to the ground state.[33]

More recent experiments with a substantially improved time resolution revealed that the early solvation dynamics occur on a much shorter time scale.[52-55] In these experiments, it was found that the ∼300-fs decay is preceded by the dynamics on a time scale of less than 50 fs. Interestingly, both experiments with 35-fs pulses[54,55] and with 13-fs pulses[52,53] pointed to the librational nature of this initial solvation dynamics. It became evident, however, that even shorter pulses are required to match the large spectral width of the hydrated electron absorption. The rapid progress of state-of-the-art laser technology in the past years has made such pulses available for spectroscopic experiments.[56-60]

In this paper we report the latest results on the early dynamics of the hydrated electron obtained with an unprecedented time resolution of 5-fs pulses. Based on the comparison of photon echo signals from hydrated electrons and from water alone, we derive a 1.6 fs pure dephasing time of the hydrated electrons. This value is fully consistent with the line shape of the absorption spectrum, which is shown to be overwhelmingly homogeneously broadened. We demonstrate that the optical response of the hydrated electron is substantially delayed with respect to the excitation pulses. This unexpected effect is explained using a model in which the transition dipole moment of the electron increases after the excitation due the strong coupling to the solvent molecules. Furthermore, it is shown that the effect is librational in nature. Finally, we demonstrate that a simple model based on wave packet dynamics can account for the experimental results.

The use of extremely short 5-fs pulses provides obvious advantages to a spectroscopic experiment. Next to the very high temporal resolution, the broad bandwidth associated with short pulses allows covering an impressive spectral window at once. On the other hand, any experiment with 5-fs pulses is a daunting task. Besides the trivial experimental nuisances such as the pulse lengthening during its propagation before and inside the sample because of group velocity dispersion, there are also more fundamental problems to be addressed.

The conventional description of nonlinear signals applicable to multi-cycle pulses becomes questionable for the pulses that consist merely of a couple of optical fringes. Clearly, in the latter case the conventionally employed slowly varying envelope approximation,[61-64] implying that the change of the pulse amplitude on the duration of an optical cycle is negligible compared to the magnitude of the amplitude itself, can no longer be maintained. Furthermore, the phase-matching bandwidth,[65,66] which is limited due to dispersion in the nonlinear medium, rapidly gains importance with the broadening of the pulse spectrum. Another point of serious concern is the frequency-dependent variation in the sensitivity of the photodetector employed to register the signal generated in the nonlinear process. In combination, the above listed features of an experiment with broadband pulses result in what is known as a spectral-filter effect.[67-69] On top of that, artificial lengthening of the observed time dependencies is a direct consequence of the noncollinear geometry employed in spectroscopic experiments. Evidently, if a portion of the signal field is filtered out in frequency and/or the signal is artificially "blurred" in time this might crucially influence the measured data[70] and subsequently lead to its erroneous interpretation.

To address these issues, we present a comprehensive theoretical analysis in which the frequency formalism and time-domain formalism of ultrafast nonlinear spectroscopy are thoroughly reexamined. The complete expressions valid even for single cycle pulse applications are derived for the nonlinear signal in the frequency and time domains. Among others, we show that one does not need to invoke the slowly varying envelope approximation in its aforementioned meaning, i.e., rejecting derivatives of the time-domain electric field. We also assert that

Photoexcited Hydrated Electron Dynamics

J. Phys. Chem. A, Vol. 103, No. 49, 1999 **10067**

the influence of geometrical delay smearing does not introduce a significant distortion of the observed traces provided that the geometry is carefully optimized.

This paper is organized as follows. In section 2, we discuss the formalism for optical four-wave mixing spectroscopy with extremely short laser pulses that consist of only a few optical cycles. We summarize the experimental conditions required to link the time- and frequency-domain observables, and discuss the impact of beam geometry on the outcome of the spectroscopic measurements with 5-fs pulses. In section 3, we describe the experimental setup for the ultrafast photon echo spectroscopy and give a detailed account on the preparation of equilibrated hydrated electrons. In section 4, the results of two- and three-pulse transient nonlinear spectroscopy on electron in ordinary and deuterated water are presented. Subsequently, a model is presented that satisfactorily explains the observed behavior. Finally, in section 5, we summarize our findings.

## 2. Ultrafast Spectroscopy with 5-fs Resolution

In this section, we derive the master equation that describes spectroscopic observables and is valid even for single-cycle optical pulses. Using the frequency-domain framework, we consistently include the effects of phase-matching, dispersive pulse broadening, dispersion of the third-order nonlinearity, and frequency dependence of the resulting nonlinear signal.

The frequency-domain formalism is then recast in the time-domain which is conventionally used in the description of transient spectroscopy with short light pulses. We subsequently show that, despite the ultrabroad bandwidth associated with 5-fs pulses, the effect of spectral filtering can be disregarded under proper experimental conditions. This allows a straightforward transition from the frequency-domain representation to the time-domain one, with the latter offering a simpler formalism. Most importantly, this simplifies the experimental task by lifting the otherwise unavoidable necessity to frequency resolve the signals generated by the ultrabroadband pulses.

2.1. The Formalism. We consider the case of noncollinear geometry in which three beams $E_i(z,t)$ ($i = 1-3$) intersect at small angles in a nonlinear medium (Figure 1). The corresponding configurations for two types of noncollinear third-order experiments are depicted in Figure 1b and 1c. The self-diffraction (SD, Figure 1b) and transient grating (TG, Figure 1c) signals are equivalent to the two- and three-pulse stimulated photon echo signals originating from the systems with phase memory. Focusing conditions of the beams are chosen such that the confocal parameter[65] and the longitudinal beam overlap of the fundamental beams are considerably longer than the interaction length. For simplicity, we assume that neither of the fields is absorbed in the nonlinear medium and that the nonlinear response is purely third order. The input beams induce then a third-order nonlinear polarization $P^{(3)}(z,t)$ that serves as a source for the signal field $E_4(z,t)$. By writing both $P^{(3)}(z,t)$ and $E_4(z,t)$ as a Fourier superposition of monochromatic waves, one obtains an equation that governs propagation of the signal wave in the $+z$ direction inside the nonlinear medium[71]

$$\frac{\partial^2}{\partial z^2}\tilde{E}_4(z,\Omega) + k_{4z}^2(\Omega)\tilde{E}_4(z,\Omega) = -\mu_0\Omega^2\tilde{P}^{(3)}(z,\Omega) \quad (1)$$

where $\tilde{E}_4(z,\Omega)$ and $\tilde{P}^{(3)}(z,\Omega)$ are Fourier transforms of $E_4(z,t)$ and $P^{(3)}(z,t)$, respectively, Ω is the frequency and $k_{4z}(\Omega)$ is the projection of the wave vector of signal field $k_4^2(\Omega) = \Omega^2\epsilon_0\mu_0\tilde{\epsilon}(\Omega)$ onto the z-axis, with $\tilde{\epsilon}(\Omega)$ being the Fourier transform of the complex relative permittivity $\epsilon(t)$.
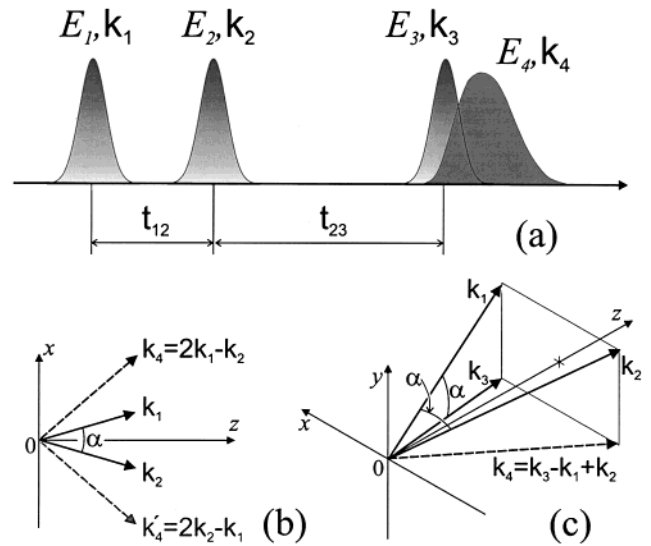
Figure 1. (a) Schematic representation of the pulse sequence in a three-pulse nonlinear spectroscopic experiment. $E_{1,2,3}$ are the input fields, and E_4 is the signal due to the third-order nonlinear process, and t_{12} and t_{23} are the delay between pulses E_1-E_2 and E_2-E_3, respectively. (b) Self-diffraction (two-pulse photon echo) configuration. Two conjugated signals are emitted in the directions k_4 and k_4'. (c) Transient grating in a "box" geometry.

To simplify the left part of eq 1, we write the signal field as a plane wave propagating along the z-axi

$$\tilde{E}_4(z,\Omega) = \bar{E}_4(z,\Omega)\exp[ik_{4z}(\Omega)z] \quad (2)$$

and substitute it into eq 1

$$2ik_{4z}(\Omega)\frac{\partial}{\partial z}\bar{E}_4(z,\Omega) + \frac{\partial^2}{\partial z^2}\bar{E}_4(z,\Omega) =$$
$$-\mu_0\Omega^2\tilde{P}^{(3)}(z,\Omega)\exp[-ik_{4z}(\Omega)z] \quad (3)$$

We now neglect the second-order derivative over the signal electric field[65,71]

$$\left|\frac{\partial}{\partial z}\bar{E}_4(z,\Omega)\right| \ll |2k_{4z}(\Omega)\bar{E}_4(z,\Omega)| \quad (4)$$

which is known as the slowly varying amplitude approximation. Note, that the use of the time-domain description of the signal wave propagation results in a second-order differential equation, similar in structure to eq 3. Unlike eq 3, though, simplification of the time-domain expression requires a rejection of the second-order *temporal* derivative of the envelope, i.e., $|(\partial^2/\partial t^2)E(t)| \ll |(4\pi/T_{per})(\partial/\partial t)E(t)|$, where T_{per} is the characteristic period of light oscillation. Such a move implies the assumption of the slow envelope variation as a function of time. This condition is not fulfilled for pulses that carry only a few cycles, since the change of the envelope within one optical period is comparable to the magnitude of the envelope itself. Brabec and Krausz,[64] who explored the time-domain approach for the propagation of nearly monocycle pulses, found out that the rejection of the second-order derivative term is warranted in the case when the phase and the group velocities of light are close to each other. To this point we notice that the application of nonequality (eq 4) to the frequency-domain (eq 3) does not require any assumptions on the change of the temporal envelope altogether. Therefore, nonequality (eq 4) is safe to apply even to monocyclic pulses, provided there is no appreciable linear absorption at lengths comparable to the wavelength.

$$\tilde{E}_4(L,\Omega) = i\frac{c\mu_0\Omega}{2n_4(\Omega)}\int_0^L \tilde{P}^{\langle 3\rangle}(z,\Omega)\exp(-k_{4_z}(\Omega)z)dz \quad (5)$$

where $n_4(\Omega) = \sqrt{\tilde{\epsilon}(\Omega)}$ is the refractive index for the signal wave and L is the thickness of the nonlinear medium.

To calculate the third-order dielectric polarization induced at frequency Ω by the fundamental fields, we should sum over all possible permutations of fundamental frequencies weighted according to the third-order susceptibility:[72]

$$\tilde{P}^{\langle 3\rangle}(z,\Omega) =$$
$$\int\int d\omega' d\omega'' \tilde{\chi}^{\langle 3\rangle}(\omega_{eg}-\omega',\omega'-\omega'',-\omega_{eg}+\Omega)\tilde{E}_1^*(z,\omega') \times$$
$$\tilde{E}_2(z,\omega'')\tilde{E}_3(z,\Omega-\omega''+\omega')\exp[i(-k_{1_z}(\omega') +$$
$$k_{2_z}(\omega'') + k_{3_z}(\Omega-\omega''+\omega'))z] \times$$
$$\exp[-i\omega'' t_{12}-i(\Omega-\omega''+\omega')(t_{12}+t_{23})] \quad (6)$$

where $\tilde{E}_i(z,\omega'')$ is a Fourier transform of $E_i(z,t)$ with their **k**-vectors represented analogously to eq 2, t_{12} and t_{23} are delays between pulses E_1-E_2 and E_2-E_3, respectively. In the SD case (Figure 1b) t_{23} is set to zero and t_{12} is scanned while in the TG experiment (Figure 1c) $t_{12} = 0$ and t_{23} is scanned. Representation of the frequency-dependent nonlinear susceptibility $\tilde{\chi}^{\langle 3\rangle}(\omega_{eg}-\omega',\omega'-\omega'',-\omega_{eg}+\Omega)$ is based on the interaction of the input fields with an electronic transition with the frequency ω_{eg}. The inclusion of the third-order susceptibility due to Raman and two-photon processes is also straightforward. The particular expression for $\tilde{\chi}^{\langle 3\rangle}$ will be discussed below.

To calculate the signal field, one should integrate the signal intensity over the longitudinal coordinate z according to eq 5. This can be performed analytically for a low-efficient nonlinear process ($E_{1,2,3}$ = const), as it is usually the case in spectroscopic applications

$$\tilde{E}_4(\Omega,t_{12},t_{23}) =$$
$$i\frac{c\mu_0\Omega L}{2n_4(\Omega)}\int\int d\omega' d\omega'' \tilde{\chi}^{\langle 3\rangle}(\omega_{eg}-\omega',\omega'-\omega'',-\omega_{eg}+\Omega) \times$$
$$\tilde{E}_1^*(\omega')\tilde{E}_2(\omega'')\tilde{E}_3(\Omega-\omega''+\omega')\,\mathrm{sinc}\Big(\Delta k_z(\Omega,\omega',\omega'')\frac{L}{2}\Big) \times$$
$$\exp\Big[i\Delta k_z(\Omega,\omega',\omega'')\frac{L}{2}-i\omega'' t_{12} - i(\Omega-\omega''+\omega')(t_{12}+t_{23})\Big]$$
$$(7)$$

The phase mismatch

$$\Delta k_z(\Omega,\omega',\omega'') =$$
$$-k_{1_z}(\omega') + k_{2_z}(\omega'') + k_{3_z}(\Omega-\omega''+\omega') - k_{4_z}(\Omega) \quad (8)$$

should be calculated for each particular geometry, given in Figure 1b,c.

Equation 7, which will be extensively used throughout this paper, is valid even for single-cycle optical pulses. The frequency representation allows us to include in a self-consistent way dispersive broadening of interacting pulses and frequency-dependence of the nonlinear susceptibility. Besides, we avoid the introduction of the carrier frequency[73] the definition of which becomes confusing for a few cycle pulses. We also draw attention to the Ω term in front of the integral that follows directly from the Maxwell equations and reflects the fact that higher frequencies are generated more efficiently. It is this term that is responsible for the effect of self-steepening of the pulses propagating in optical fibers.[74]
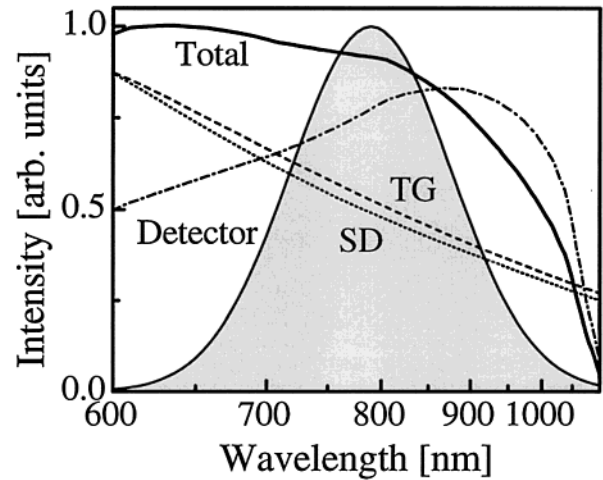
Figure 2. Spectral filters for two configurations of photon echo in water. Shaded contour represents the spectrum of ideal 5-fs pulses. The spectral filter calculated for self-diffraction is shown by a dotted line, and the filter for transient grating is presented by a dashed line. The dash−dotted line depicts the typical spectral sensitivity of a silicon light detector, $Q(\lambda)$. The spectral filter for transient grating corrected by $Q(\lambda)$ is given by a solid curve. The thickness of the water layer is taken as 100 μm, and the intersection angles of the beams are 4°. Note that the overall spectral filter (solid curve) is nearly flat up to 900 nm due to the photodetector sensitivity balancing off the more efficient generation of the nonlinear signal at higher frequencies.

The total spectrally resolved signal registered by a quadratic detector is written as

$$\tilde{I}_4(\Omega,t_{12},t_{23}) = \epsilon_0\frac{n_4(\Omega)Q(\Omega)}{c}|\tilde{E}_4(\Omega,t_{12},t_{23})|^2 \quad (9)$$

with $Q(\Omega)$ being the spectral sensitivity of a monochromator−detector combination.

From the point of view of practical application of 5-fs pulses, we now quantify the differences between the complete frequency-resolved signals of TG and SD computed according to eqs 7−9 with $\tilde{\chi}^{\langle 3\rangle}$ = const and the ideal frequency-resolved TG and SD signals for an instantaneous nonlinear response[75]

$$I_4^{\mathrm{ideal}}(\Omega,t_{12},t_{23}) = |\int\int d\omega' d\omega'' \tilde{E}_1^*(z,\omega')\tilde{E}_2(z,\omega'')\tilde{E}_3(z,\Omega-$$
$$\omega''+\omega')\mathrm{e}^{-i\omega'' t_{12}+i(\omega''-\omega')(t_{12}+t_{23})}|^2 \quad (10)$$

The comparison of the respective complete and ideal signals provides us with information on the spectral filter effect, a combined influence of the spectral variations in the generation efficiency of the signal field and in its detection. To simulate our experimental conditions, in the calculation of the complete SD and TG traces we included dispersive properties of a 100-μm layer of water[76,77] and the impact of the noncollinear beam geometry on the phase mismatch given by eq 8. The ideal frequency-resolved traces were calculated according to eq 10. The spectral filters for the SD and TG cases, obtained as the ratios of the complete (eqs 7−9) vs ideal (eq 10) signals, are presented in Figure 2. The dashed and dotted curves correspond to TG and SD, respectively, for the case of a flat spectral response of the detector ($Q(\Omega)$ = const). Apparently, both filters are dominated by the Ω^2 dependence that originates from the Ω term in eq 5. The curvature of the SD filter compared with the TG one is somewhat steeper. This reflects the fact that the phase mismatch for SD is greater since SD is intrinsically nonphase-matched geometry.[75]

Photoexcited Hydrated Electron Dynamics

J. Phys. Chem. A, Vol. 103, No. 49, 1999 **10069**

The taking into account of a typical real spectral sensitivity of a silicon photodiode, $Q(\Omega)$ (dash−dotted curve in Figure 2) results in the overall spectral filter for TG depicted by a solid curve. Noteworthy, the overall spectral filtering effect is nearly frequency-independent throughout most of the spectrum of a 5-fs pulse (shaded contour in Figure 2) because the photodetector sensitivity balances off the Ω^2 dependence. Therefore, we can disregard the effect of spectral filtering in case it is counterweighed by the spectral response of a properly chosen detector. This is an important conclusion for the practical purpose of nonlinear spectroscopy with 5-fs pulses since it justifies the use of less cumbersome spectrally unresolved detection of TG and SD signals.

Now we demonstrate how to arrive to the conventionally used time-domain description of ultrafast spectroscopy.[66] As we already pointed out, to match the information obtained in a SD or TG experiment, eq 9 should be integrated over all frequency components in order to obtain the total energy of the signal field detected by a quadratic detector. According to Parseval's theorem,[78] the amount of energy carried by the signal is the same whether we compute it in the time domain or in the frequency domain. Therefore, the following formula is a time-domain expression for the same signal:

$$S(t_{12},t_{23}) = \epsilon_0 \frac{n(\omega_4)}{2\pi c} \int_{-\infty}^{\infty} dt |E_4(t,t_{12},t_{23})|^2 \quad (11)$$

where

$$E_4(t,t_{12},t_{23}) = \frac{c\mu_0 L}{2n_4(\omega_4)} \int_0^\infty \int_0^\infty \int_0^\infty dt_1 dt_2 dt_3 E_1^*(t - t_3 - t_2 - t_1) E_2(t - t_{12} - t_3 - t_2) E_3(t - t_{23} - t_{12} - t_3) R(t_1,t_2,t_3)$$
$$\exp[-i\omega_{eg}(t_3 - t_2) + i(\omega_3 + \omega_2 - \omega_1)t_3 + i(\omega_2 - \omega_1)t_2 - i\omega_1 t_1 + i\omega_2 t_{12} + i\omega_3(t_{12} + t_{23})] \quad (12)$$

and the so-called nonlinear response function is introduced as a Fourier transform of the nonlinear susceptibility[66]

$$R(t_1,t_2,t_3) = \int\int\int \tilde{\chi}^{(3)}(\omega_1,\omega_2,\omega_3) \exp[-i\omega_1 t_1 - i\omega_2 t_2 - i\omega_3 t_3] d\omega_1 d\omega_2 d\omega_3 \quad (13)$$

In eq 12 we also extracted the oscillations of electrical fields at the optical frequency ω_i

$$E_i(t) = E_i(t) \exp(-i\omega_i t) \quad (14)$$

Note, that in the case of ultrabroadband optical pulses the transition between the frequency-domain description formulated by eqs 7−9 and the time-domain representation summarized by eq 11−13 becomes valid only in the case of a flat spectral filter. In other situations when the spectral filtering of the SG or TG signals does occur (regardless of its reason), the correctness of eq 12 is not warranted and one must use more general eqs 7−9. The distortion of measured time-dependencies due to spectral filtering is well known from the example of second harmonic autocorrelation in the $\tilde{\chi}^{(2)}$ crystals with finite thickness.[67]

Equation 13 provides the link between the nonlinear response function $R(t_1,t_2,t_3)$ and the third-order susceptibility $\tilde{\chi}^{(3)}$. For the former, extensive formalism of non-Markovian dynamics, based on the pathway propagation in the Liouville space[66] has been developed. Here we restrict ourselves to a simple model of a homogeneously broadened two-level system. In this case, the nonlinear response function is given as

$$R(t_1,t_2,t_3) = \frac{\mu_{eg}^4 N}{\hbar^4} \exp\left[-\frac{t_1 + t_3}{T_2} - \frac{t_2}{T_1}\right] \quad (15)$$

where μ_{eg} is the transition dipole moment, N is concentration, T_1 and T_2 are the population relaxation and dephasing times, respectively, and

$$T_2^{-1} = (T_2^*)^{-1} + (2T_1)^{-1} \quad (16)$$

with T_2^* being the pure dephasing time. Fourier transformation of eq 15 yields a well-known result[79]

$$\tilde{\chi}^{(3)}(\omega_{eg} - \omega',\omega'-\omega'',-\omega_{eg} + \Omega) =$$
$$-i\frac{\mu_{eg}^4 N}{\hbar^4} \frac{1}{T_1^{-1}-i(\omega''-\omega')}\left[\frac{1}{T_2^{-1}-i(\omega_{eg} - \omega')} + \frac{1}{T_2^{-1}-i(\omega''-\omega_{eg})}\right]\frac{1}{T_2^{-1} + i(\omega_{eg} - \Omega)} \quad (17)$$

The second sum term in square brackets in eq 17 is included to account for the fact that $\tilde{\chi}^{(3)}$ possesses symmetry with respect to ω' and ω'', and the total expression of $\tilde{\chi}^{(3)}$ is a sum of all frequency permutations.[71,65] Third-order susceptibilities for different four-photon processes such as Raman scattering or two-photon absorption can be calculated in a similar fashion. The two-level system can also be dressed in a vibrational manifold to account for coherent excitation of several Franck−Condon transitions.[66]

2.2. Ultimate Temporal Resolution of SD and TG Experiments. In this section we address geometrical smearing − the effect deteriorating the temporal resolution of a nonlinear spectroscopic experiment as a direct consequence of employing noncollinear beam geometry. This type of distortion originates from the fact that in a beam, inclined at an angle to a plane, different transverse components of a pulse travel different distances before reaching the plane. This means that a fixed delay between two pulses propagating in two intersecting beams changes into a range of delays across the waist of the beams in the intersection region. The very same idea of yielding a range of delays simultaneously is utilized in single-shot pulse autocorrelation techniques.[80]

The described above "delay blurring" can be of a serious concern dealing with the laser pulses that have duration shorter than 10 fs. This issue has been addressed previously in connection with the temporal resolution of a noncollinear pulse duration measurement via second-harmonic generation.[68,69] Analogously to ref 69, here we evaluate the influence of the geometrical smearing on the width of self-diffraction and transient grating traces.

For arbitrary pulses and beam profiles, the shape of the resulting traces should be computed numerically by integrating eq 9 over each transverse component of the beam. For linearly chirped Gaussian pulses with Gaussian spatial profile, however, these traces can be calculated analytically. Assuming that the nonlinear response of the medium is instantaneous, one can calculate from eq 10 that the ideal SD or TG trace has a Gaussian intensity profile in time. Its width, τ_0, is by a factor of $\sqrt{3/2}$ broader than the pulse duration. The width of the actual signal, τ_{meas}, which has been stretched by geometrical smearing, can be expressed by

$$\tau_{meas}^2 = \tau_0^2 + \beta\delta^2 \qquad (18)$$

where β is a scaling constant dependent on the employed beam geometry and δ is the effective delay smearing given by

$$\delta = \frac{\alpha d_f}{2c} \qquad (19)$$

Here d_f is the beam diameter in the focal plane and α is a small intersection angle between the interacting beams (Figure 1b,c). As has been reported in ref 69, the lowest value of δ for Gaussian pulses and beams amounts to 0.4 fs if the central wavelength of the pulse is 800 nm. For the beam profiles other than Gaussian the value of δ becomes larger.

For self-diffraction the constant β equals 4/3, while for transient grating in the "Box" beam arrangement β takes the value of $\approx$5/3. The influence of geometrical smearing on the width of the trace observed in these two measurement configurations is illustrated in Figure 3. As can be seen from Figure 3, the temporal resolution of the self-diffraction experiment is somewhat higher compared to transient grating. This is explained by the fact that the smearing in the case of transient grating takes place in xz and yz planes (Figure 1c) simultaneously. In any case, for intersection angles smaller than 10° the lengthening of the detected signal does not exceed 10%.

Therefore, the effect of geometrical smearing on the generated signals is insignificant even for experiments with pulses as short as 5 fs, provided the intersection angle is kept sufficiently small and the beams are properly focused.

3. Experimental Section

3.1. Femtosecond Laser System. The femtosecond spectrometer is based on a home-built cavity-dumped Ti:sapphire laser, that has been described in detail elsewhere.[57] The schematics of the setup is presented in Figure 4. Briefly, the cavity-dumped laser is a standard Ti:sapphire oscillator that incorporates a Bragg cell inside the cavity. This allows us to produce 15-fs pulses at the central wavelength of 790 nm at a desired repetition rate. The energy of the dumped pulses reaches up to 35 nJ and is adjustable by setting a level of RF power applied to the Bragg cell.

To provide adequate time resolution for the study of the ultrafast dynamics of the hydrated electron and broaden the spectral window of our measurements, the output of the cavity-dumped laser is externally compressed to the pulse duration below 5 fs.[57] The 15-fs laser pulses, precompressed by a pair of fused silica prisms, are injected into a single-mode quartz fiber through a microscope objective lens. The white-light continuum resulting from the combined action of the self-phase modulation and dispersion in the fiber core is collimated by an off-axis parabolic mirror to avoid chromatic aberrations and bulk dispersion of a collimating lens. A portion of the white-light in the spectral range of 580−1060 nm (shaded contour in Figure 5) is then compressed in a state-of-the-art three-stage pulse compressor that includes a pair of 45° quartz prisms, specially designed chirped dielectric mirrors, and thin-film dielectric Gires-Tournois interferometers.

Immediately before performing photon echo spectroscopy on hydrated electrons, the compressor is adjusted to yield the shortest duration of the pulses, which are characterized by second-harmonic frequency-resolved gating (SHG FROG).[69] Because dispersive broadening easily affects the 5-fs pulses, even as they propagate through air, the FROG characterization is carried out directly at the location of the spectroscopic sample
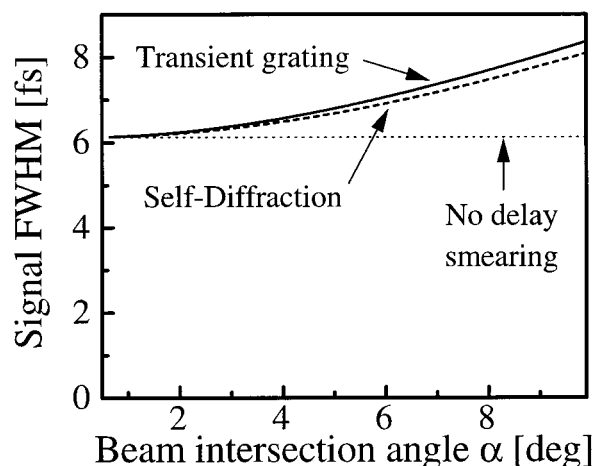
Figure 3. Geometrical smearing of transient grating and self-diffraction traces as a function of beam intersection angle. The temporal widths of the observed signals are shown by solid and dashed curves for transient grating and self-diffraction, respectively. The duration of ideal Gaussian pulses is 5 fs and the nonlinear response is assumed instantaneous. The focal length of the focusing optics is 125 mm and the fwhm of the collimated Gaussian beams is 2 mm.

by replacing it with a very thin (10 μm) second-harmonic BBO crystal (EKSMA).

3.2. Transient Grating and Photon Echo Experiments. The experimental arrangement used for the photon echo spectroscopy is depicted in Figure 4. The beam carrying 6-nJ, 5-fs pulses is split into three channels of approximately equal intensity by the 0.5-mm-thick beam splitters BS1 and BS2 (pulses E_1, E_2, and E_3 in Figure 4). Compensating plates (CP) of the same thickness are inserted into the beams to equalize dispersion in all three channels. To minimize distortions in the pulse duration and preserve its spectral content, silver mirrors overcoated by a thin protective layer are used throughout. To match the reflectivity of the beam splitters, the initial horizontal polarization of the laser beam is turned 90° by a mirror periscope. The optical polarization of one of the pulses, E_3, is further turned by 45° with respect to the polarization of the pulses E_1 and E_2 by another periscope to facilitate photo-echo measurements in the parallel and orthogonal polarization directions. Two independent optical delay lines, t_{12} and t_{23}, are employed to generate desired sequences of the three pulses.

Transient gratings in the sample are formed by focusing the three beams into a 100 μm jet carrying the hydrated electrons. The grating response is detected by collimating the emerging beams using spherical mirrors with a radius of curvature R = −250 mm. A small incidence angle on the spherical mirror is chosen to prevent astigmatism of the beams within the intersection region. The intersection angles between the incident beams are kept at ∼4°. The waist of the focused beam is ∼30 μm in diameter. The phase-matching geometry of the laser beams is explained in the bottom-left inset to Figure 4, presenting the enlarged image of the beam configuration on the recollimating mirror. The advantages of employing such a beam arrangement have been discussed previously.[81]

The two- and three-pulse stimulated echo signals are detected simultaneously behind the sample by silicon photodiodes PD1−4 equipped with built-in amplifiers. The photodiode signals are processed by lock-in amplifiers, digitized, and stored in the computer memory.

The ability to determine the exact overlap of the pulses E_1−E_3 in time with a high degree of precision presents a considerable experimental challenge and is vital for the photon echo
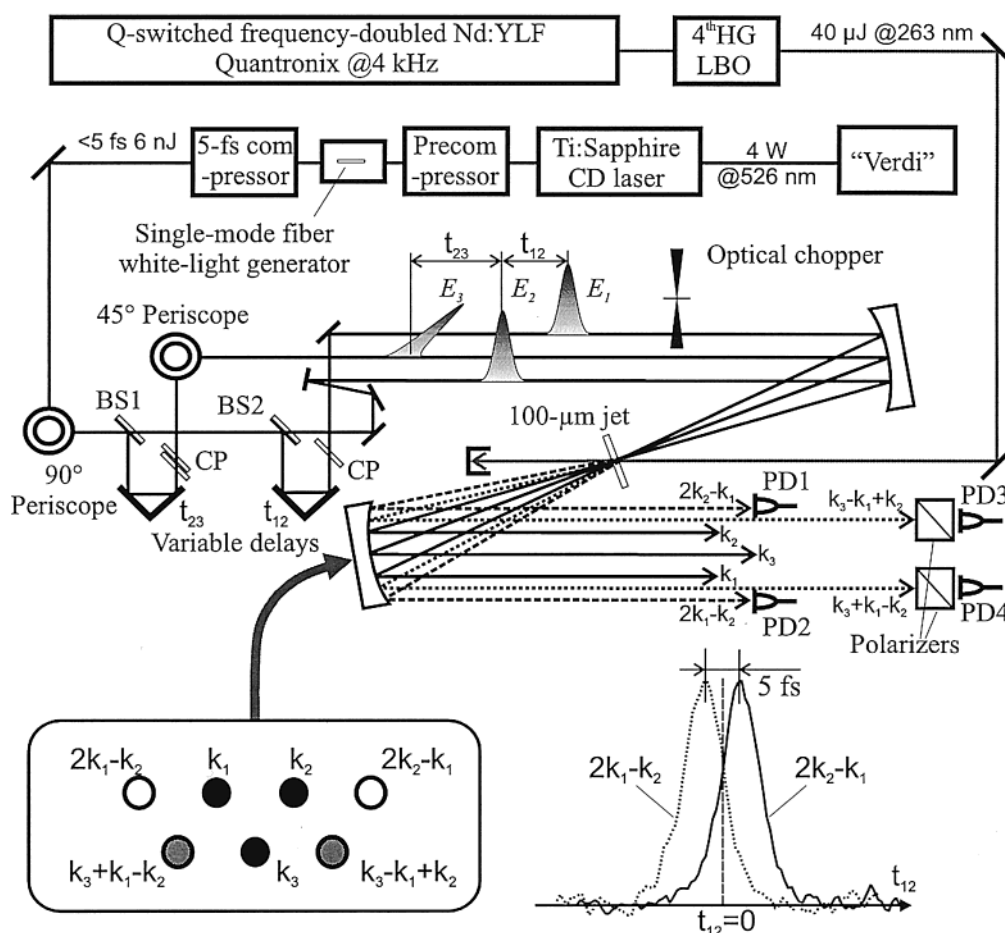
Figure 4. Schematics of the femtosecond photon echo spectrometer. BS1 is an $R = 30\%$ beam splitter, BS2 is a 50% beam splitter. CPs are compensating plates and PD1−4 are silicon light detectors. E_1, E_2, and E_3 are femtosecond excitation pulses and t_{12} and t_{23} are the delays between pulses E_1−E_2 and E_2−E_3, respectively. The bottom-left inset shows the image of the signal and excitation beam arrangement on the recollimating mirror. The bottom-right inset shows the profiles of two-pulse photon echoes measured in two conjugate directions by PD1 and PD2.
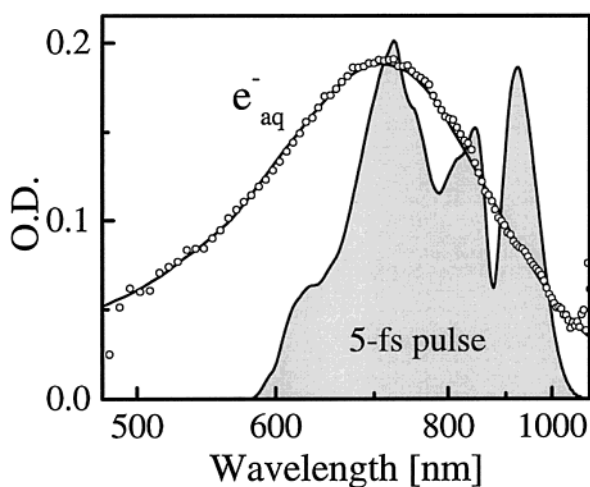
Figure 5. Absorption spectrum of electrons in water. The solid line is the absorption of hydrated electrons produced by electron beams in bulk water (adopted from ref 32). The solid dots are measured with the femtosecond white-light continuum upon photoionization of potassium ferrocyanide with 263-nm pulses. The shaded contour shows the spectrum of the 5-fs pulses.

measurements with 5-fs pulses that occupy merely 1.5 μm in space. Fortunately, the overall symmetry of the employed configuration makes it possible to accurately find $t_{12} = 0$ and $t_{23} = 0$ without employing additional means.

The two-pulse photon echo traces are measured as a function of delay between the pulses E_1 and E_2. A typical result of a t_{12} scan is depicted in the bottom-right inset to Figure 4. Here the solid and the dashed curves represent the contours obtained in the two conjugate directions, monitored by the photodiodes PD1 and PD2, respectively. Since these two-pulse photon echo traces are intrinsically symmetric around $t_{12} = 0$, such a scan allows finding the precise overlap of the pulses E_1 and E_2. Similarly, the precise location of $t_{23} = 0$, i.e., the overlap between the pulses E_2 and E_3 can be verified by a t_{12} scan of the three-pulse echo signals, which in the case of coinciding pulses E_2 and E_3 correspond to the signals depicted in the inset to Figure 4.

The transient grating scans, a variety of three-pulse photon echo spectroscopy, are performed by scanning the delay t_{23} between the time-coincident pair of excitation pulses E_1−E_2 and the third (probe) pulse E_3. The symmetry of the incident beam arrangement implies that, in this case, two exactly identical signals are emitted in $k_3+k_2-k_1$ and $k_3-k_2+k_1$ directions. This also serves as a sensitive indicator to continuously monitor the perfect time overlap of the excitation pulses. By rotating polarizing cubes in front of PD3−4 we record the components of the transient grating signal parallel and perpendicular to the polarization of the pulses E_1 and E_2.

3.3. Generation of Hydrated Electrons. The technique of hydrated electron generation through electron photodetachment from various types of anions[82] has been introduced almost immediately following the observation of hydrated electron formation by the action of intense electron beams on water.[3,4]

The former production method offers a clear advantage, since it typically requires merely one-photon ionization and, therefore, is employed in our experiments. Among different complex ions, studied for the electron photodetachment,[82-85] ferrocyanide (hexacyanoferrate(II), $Fe(CN)_6^{4-}$) was found to have the highest quantum yield, reaching the value of 0.9 for 228-nm irradiation.[86] In the case when a ferrocyanide ion is photolyzed to yield a hydrated electron, an $Fe(CN)_6^{3-}$ ion, hexacyanoferrate(III), forms in the solution which gives rise to an absorption band at 415 nm.[83,87] The important fact that the absorption of this photoproduct clearly lies outside the spectral range of our femtosecond experiment, is an additional favorable aspect of employing ferrocyanide rather than another negative ion.

Hydrated electrons are generated by photoionizing a small amount of potassium ferrocyanide[55,82,86,88] added to water, with the quadrupled output of a Nd:YLF laser (263 nm). Potassium ferrocyanide was obtained from Merck. Water and heavy water of HPLC grade were purchased from Aldrich and used without further purification. The polished sapphire nozzle (Kiburtz) ensured good quality of the jet and, therefore, no addition to the solution of the chemical substances stabilizing the jet surfaces[55] was needed. All measurements were carried out at room temperature.

The repetition rate of the YLF laser and, consequently, the repetition rate of the entire spectrometer was set at 4 kHz. The UV pulses are focused directly into the intersection region of the pulses E_1, E_2, and E_3 in the water jet. To avoid noticeable variation of electron concentration within the interaction area of the femtosecond pulses, the spot size of the UV beam on the water jet is approximately two times larger than the waist of the three other beams. The triggering of the Nd:YLF laser is synchronized with the cavity-dumping of the Ti:sapphire laser so that the UV pulse precedes the femtosecond pulse by ~200 ns. The absorption spectrum of hydrated electrons has been measured in the spectral region 480–1100 nm with uncompressed white-light pulses and obtained as a difference in optical density of the water jet in the presence of, and without, UV radiation. The typical absorption spectrum (Figure 5, open circles) has the peak value of o.d. ≈ 0.2 around 720 nm. The data of our absorption measurement coincide very well with the known from the literature[32] absorption spectrum of hydrated electrons (Figure 5, solid line) that have been directly injected into a volume of water.

Unlike the injected electrons which reportedly in water have a lifetime of ~10 μs,[4] the electrons released through photoionization generally have a shorter recombination time. The mechanism responsible for this shortening is a so-called scavenging process, whereby an electron recombines with one of the ions of the donor molecules or other scavengers introduced to the solution.[85] Thus, the variation of the concentration of ferrocyanide in the solution has a two-side effect. On one hand, the increase of the concentration is directly proportional to the amount of electrons generated by photoionization. On the other hand, it increases the rate of electron recombination with the ferrocyanide ions because of the scavenging. To measure the recombination time, we recorded the change in absorption of the hydrated electrons as a function of delay between the photoionizing UV pulse and the white-light pulse. The normalized kinetics at 720 nm obtained at two different concentrations of ferrocyanide are depicted in Figure 6 as circles. The intensity profile of the 120-ns UV pulse shown alongside (shaded contour) was detected with a fast solar-blind photomultiplier tube (Hamamatsu) and recorded with a 1-GHz sampling oscilloscope (Hewlett-Packard). The delay between
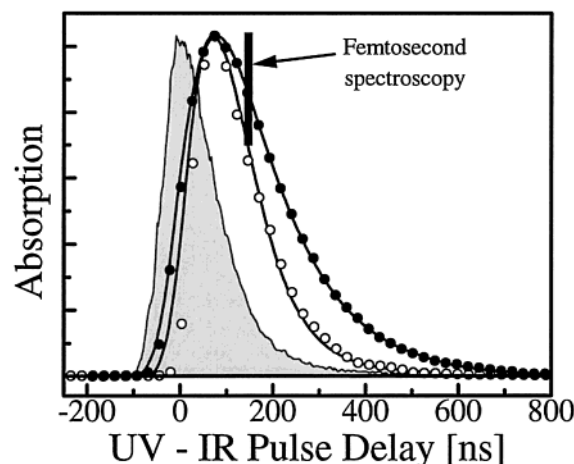
Figure 6. Recombination dynamics of hydrated electrons generated by photoionization. The shaded contour shows the intensity of the UV pulse used for photoionization. The dots represent measured and normalized absorption changes at the wavelength of 720 nm for potassium ferrocyanide concentrations of 0.4 g/L (solid circles, peak optical density ~0.2) and 4.0 g/L (hollow circles, peak optical density ~0.05). The solid curves depict the fits obtained according to the procedure described in the text.

the two pulses was set electronically by varying the triggering time of the Ti:sapphire and the Nd:YLF lasers in steps of 24 ns.

The photoionization process, countered by the electron scavenging, was modeled by a simple balance equation similar to the one derived in ref 85 in which we included the scavenging term and explicit pulse shape

$$\frac{dN(t)}{dt} = -\frac{N(t)}{\tau} + \alpha I_{UV}(t) \qquad (20)$$

here $N(t)$ is a concentration of equilibrated hydrated electrons, τ is the time constant of electron–ion scavenging, $I_{UV}(t)$ is the intensity of the UV pulse, and α is a constant reflecting the quantum efficiency of photoionized electron generation. In eq 20 we assumed that the hydrated electrons are formed instantaneously. Since the spectrum of the hydrated electrons is formed with a time constant of 0.3–0.5 ps,[87,89] this assumption is fair on the much slower time scale of our experiment.

Equation 20 was solved numerically to fit the data presented by circles in Figure 6. Digitized pulse shape (Figure 6, shaded contour) was used as the parameter $I_{UV}(t)$, and τ was a fitting parameter to match the experimental dependence. The respective fits of the two data sets are depicted in Figure 6 by solid lines. The decay time τ obtained for the ferrocyanide concentration $C = 0.4$ g/L is 115 ns, while for $C = 4.0$ g/L $\tau = 45$ ns. Therefore, a 10-fold increase of the ferrocyanide concentration results in an about 2-fold acceleration of the rate of electron–ion recombination, while the absorption of hydrated electrons at its peak increases by a factor of 5.

The femtosecond photon echo spectroscopy on the hydrated electrons was performed in the time window indicated on the falling edge of the absorption change traces shown in Figure 6 as a vertical bar. While the concentration of the electrons is still near its peak at this delay, the UV pulse is already largely over and, therefore, predominantly equilibrated hydrated electrons are present in the solution at this time.

3.4. Intensity-Dependence Measurements. To verify the order of the nonlinearity contributing to the transient grating signal from the hydrated electrons, we measured the dependence of this signal on the intensity of femtosecond pulses. Since the

Photoexcited Hydrated Electron Dynamics

J. Phys. Chem. A, Vol. 103, No. 49, 1999 **10073**
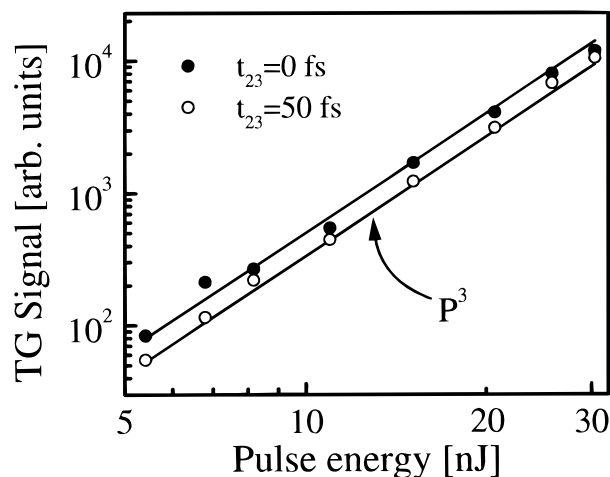
Figure 7. Intensity dependence of the transient grating signal from hydrated electrons. Closed and open circles show data measured at delays between the excitation pulse-pair and the probe pulse of t_{23} = 0 and 50 fs, respectively. The solid lines depict third-power dependencies expected for the third-order nonlinearity.

tuning of the 5-fs pulse intensity without destroying the pulse duration or its spectral content is not feasible, we employed for this purpose 15-fs pulses directly from the cavity-dumped laser. The energy of the 15-fs pulses was changed by varying the RF power of the cavity-dumper driver in the interval 5−30 nJ. This corresponds to the combined intensity of the three pulses in the sample ranging from 0.6×10^{11} to 4.0×10^{11} W/cm². The power dependencies of the TG signal (i.e, $t_{12} = 0$) from electrons in water measured at two different values of t_{23} delay are depicted in Figure 7 (dots). Solid lines shown alongside the experimental data represent the cubic power dependence that is expected from nonlinearity based on the third-order response. Clearly, no noticeable deviation from the third-power law is reached with the intensities used.

Previous intensity-dependence measurements of the pump−probe signal from hydrated electrons revealed departure from a purely third-order nonlinear response for the intensities of the excitation pulse in excess of $\sim 3.0 \times 10^{11}$ W/cm².[55] For higher intensities, leveling-off of the signal was reported. Since the pulse intensities applied in our measurement did not exceed 4.0×10^{11} W/cm², the saturation regime has not been reached yet.

The total intensity of the excitation pulses in the 5-fs experiments amounted to 2×10^{11} W/cm². Therefore, the contribution of higher-order nonlinearities or saturation effects is not expected in the experiments reported below.

The contribution of the pure water to the total nonlinear optical response of the sample was checked by recording the photon echo traces in absence of UV pulses. This contamination of the signal did not exceed $\sim 5\%$ of the signal peak value obtained in the presence of the hydrated electrons and was confined to the region of delays within the overlap of the 5-fs excitation pulses.

4. Results and Discussion

4.1. Pure Dephasing Time of Hydrated Electrons. The employed method of the generation of hydrated electrons provides us with a unique opportunity to compare the photon echo signal from the hydrated electrons with the one measured in pure water, that is, in absence of photoionizing radiation. Since electronic hyperpolarizability[90−92] heavily dominates the overall water response,[93,94] it is well justified to treat the nonlinearity as nearly instantaneous on the time scale of our
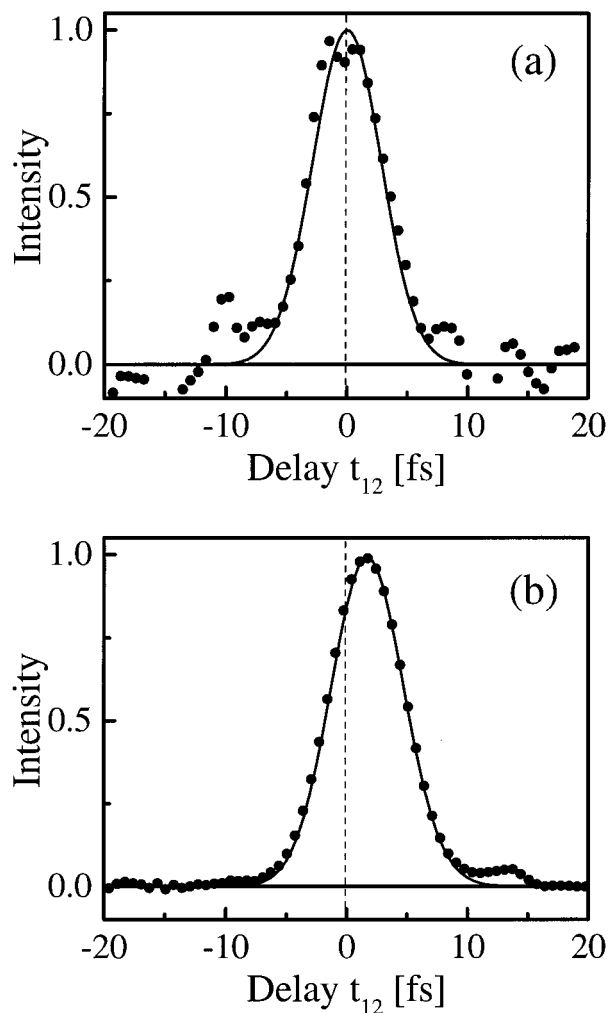
Figure 8. Results of two-pulse photon echo experiments on water alone (a) and hydrated electrons (b). Circles represent experimental data points and solid curves show fits obtained according to the procedure described in the text.

pulses. Therefore, the signals obtained from pure water correspond to the ultimate instrument response of the spectrometer. This instrument function, among its other merits, automatically accounts for the pulse duration, mode size, and spatial as well as spectral filtering in the detection. Therefore, the differences in the shape of photon echo traces recorded in the presence and without the UV radiation provide us with direct information on electronic dephasing of the hydrated electrons.

The two-pulse photon echo signals from water and hydrated electrons are shown as solid circles in Figure 8a and 8b, respectively. A minute difference in the widths of these two traces suggests that the electronic dephasing of the photoexcited hydrated electrons is extremely fast. To fit to the experimental data (solid curves in Figure 8a and 8b), we used the formalism developed in section 2. The precise pulse parameters were obtained from independent FROG characterization as described in Section 3.1. For water (Figure 8a), we assumed an instantaneous response function (eq 15) $R(t_1,t_2,t_3) \propto \delta(t_1)\delta(t_2)\delta(t_3)$ or, in other words, the frequency-independent third-order susceptibility. In the case of the hydrated electron (Figure 8a), complete eq 15 was used with the dephasing time T_2 being the fitting parameter. The population lifetime T_1 was considered to be much longer than any relevant experimental time scale, including pulse duration. Experimental evidence[54,55] supports the idea that the excited-state lifetime can be as large as hundreds

of femtoseconds. Therefore, the difference between the full electronic dephasing time, T_2, and the pure dephasing time, T_2^*, which are connected by eq 16, is negligible.

The finite population lifetime of the electrons in the excited state causes the delay of the echo trace in Figure 8b (its shift of further away from $t_{12} = 0$ compared to the data in Figure 8a). The best fit to the experimental data yields the dephasing time of $T_2 = 1.6$ fs. Note that this value is reasonably close to theoretical estimations derived from a model based on the Gaussian wave packet approximation for the bath. [39,95,96] The addition of any appreciable amount of inhomogeneity immediately results in pulling the echo maximum away from zero and appearance of noticeable asymmetry of the trace.

Evidently, such a 1.6-fs dephasing time should manifest itself in the absorption line shape which has to be substantially homogeneously broadened.[66] Here we stress that the use of a standard Lorentzian line shape is not warranted for the spectra with the widths comparable to the central frequencies. Instead, a more general relation should be used[63,65,97]

$$\sigma_A(\omega) \propto \omega \, \mathrm{Im}[\chi^{\langle 1 \rangle}(\omega)] \propto$$

$$\omega \mathrm{Im}\left[\frac{1}{(\omega_{eg} - \omega) - iT_2^{-1}} + \frac{1}{(\omega_{eg} + \omega) + iT_2^{-1}} \right]$$

$$\propto \frac{4\omega^2 T_2^{-2}}{(\omega_{eg}^2 - \omega^2)^2 + 4\omega^2 T_2^{-2}} \quad (21)$$

In eq 21 σ_A is the absorption cross section and ω_{eg} is the transition frequency. In the case of a narrow absorption band, i.e., $T_2^{-1} \ll \omega_{eg}$, one can make use of the approximation $\omega \cong \omega_{eg}$ which immediately gives the conventional Lorentzian contour

$$\sigma_A(\omega) \propto \frac{T_2^{-2}}{(\omega_{eg} - \omega)^2 + T_2^{-2}} \quad (22)$$

In fact, the rejection of the second term of the sum in eq 21, resulting in eq 22, amounts to application of the so-called rotating wave approximation (RWA).[65,66] The difference between the two line-shapes, given by eq 21 and eq 22, mostly affects the asymptotic behavior in the low-frequency spectral wings. Besides, unlike the pure Lorentz function eq 22, which produces a centrosymmetric contour, the line shape described by eq 21 is essentially asymmetric. The latter contour has a more abrupt red wing and a prolonged blue wing. The need to account for the experimentally observed asymmetry precluded the use of a single Lorentzian line shape in the past attempts to model the absorption spectrum of hydrated electrons. Consequently, a collection of spectral lines[27,31,33] or a combined line-shape[26,28,29,30,32] was required for a reasonable fit.

Employing the more general relation for a homogeneously broadened line shape given by eq 21, we obtained a fit (solid curve in Figure 9) to the absorption spectrum of electrons injected into bulk water at 298 K.[32] Evidently, the whole absorption spectrum can be excellently reproduced by a homogeneously broadened line-shape. The dephasing time $T_2 = 1.7$ fs, deduced from the fit of the spectrum, perfectly agrees with the one obtained from the photon echo experiment. This leaves no room for doubts about the homogeneous nature of spectral broadening of the hydrated electron absorption band.

Having established that the absorption spectrum of the hydrated electron is homogeneously broadened, we address the results of MD simulations from which the conclusion of
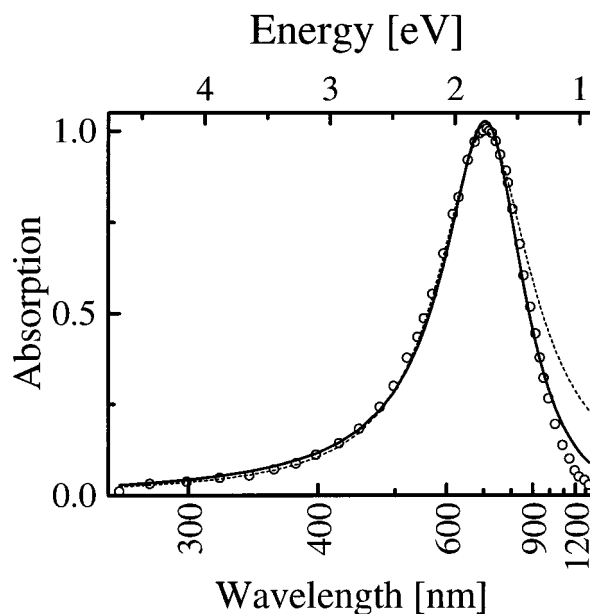
Figure 9. Fit of absorption spectrum of electrons in water. The circles show measured absorption of hydrated electrons produced by electron beams in bulk water (adopted from ref 32). The solid curve shows the fit by homogeneously broadened line-shape calculated according to eq 21. Dotted line depicts a Lorentzian line shape given by eq 22.

inhomogeneous broadening of each $s-p$ band was made.[18,23,24] It is clear that the stipulated nondegeneracy of the p-states is a direct and natural consequence of the not entirely spherically symmetric solvent cavity. However, the decomposition of the absorption spectrum into three bands seems to be somewhat artificial. Indeed, as the energy of a given p-state fluctuates in time as a result of the rearrangement of the surrounding solvent molecules, this state might well become the highest or the lowest among the three p-states. According to the proposed ordering of the excited states by energy, one should then reassign the transition to this p-state as belonging to a different absorption subband. As a consequence of this artificial reassignment, the width of the Gaussian-like subbands revealed by these simulations becomes nearly equal to the separation of the band centers (vide supra). If the energy-dependent order were dropped, the absorption band associated with each $s-p$ transition eventually would have the same width as the whole absorption spectrum of the solvated electron. This means that, depending on the current precise solvent surroundings, the optical transition to a designated p-state can take place anywhere across the whole absorption spectrum. The dynamic fluctuations of the solvent cavity cause constant "migration" of the respective $s-p$ absorption bands within the common envelope.

We state that the seeming confusion with the assignment of the three absorption subbands arose from the averaging over an ensemble of solvent configurations[18,23,24] rather than averaging of the same configuration evolving in time. The same averaging of multiple static cavity "snapshots" led to the conclusion of the inhomogeneous broadening of each absorption line.[18,23,24]

To the best of our knowledge, there has been no experimental evidence supporting the hypothesis of the inhomogeneous nature of the line broadening in the absorption of an electron in a fluid. Both picosecond[98] and femtosecond[33] transient pump-probe spectra revealed no presence of hole-burning behavior. Our recent attempts to imprint a spectral hole in the hydrated-electron absorption line employing a 15-fs excitation pulse centered around 800 nm and a broadband 5-fs readout pulse likewise

resulted in a uniform and immediate bleaching of the whole absorption contour,[99] suggesting that the latter is overwhelmingly homogeneously broadened. The lack of asymmetry in the two-pulse photon echo signal (Figure 8b) is another strong evidence in favor of overwhelming homogeneous broadening. Besides, in the TG experiments we observed no quantum beats which are usually associated with the coherent excitation of several transitions (vide infra).

Therefore, based on the current and previously accumulated experimental data we conclude that the absorption spectrum of the hydrated electron is predominantly homogeneously broad-ened. An important question now should be raised about the physical origin of a very rapid dephasing associated with a very broad absorption band. Indeed, hardly any nuclear motion on such a short time scale should be expected. However, the electronic dephasing is not necessarily the consequence of the rapid fluctuation of local structures, nor does it mean that a large amount of energy has to be dissipated by the bath within a few femtoseconds. It is well known that the difference in the frequencies of (harmonic) ground and excited-state potentials influences electronic dephasing through the so-called quadratic electron–phonon coupling.[100–104] This mechanism also has been shown to lead to prevalently homogeneous broadening of absorption lines.[105] Since multiphonon interactions are involved in nonlinear electron–phonon coupling, the latter explains large breadths of absorption spectra in the case of a relatively modest width of the spectral density of the solute–solvent fluctuations.[66]

To conclude this section, we suggest that the absorption band of equilibrated hydrated electrons is primarily *homogeneously* broadened with the corresponding dephasing time $T_2 \cong 1.6$ fs. The asymmetry of the spectrum is explained by the frequently neglected dependence of the optical absorption cross section on frequency. A mechanism responsible for the extraordinary width of the absorption spectrum is most probably the quadratic electron–phonon coupling due to appreciable difference in the steepness of the ground- and excited-state potentials.

4.2. Transient Grating Spectroscopy. The early part of TG transients of the hydrated electron is shown in Figure 10a for parallel polarizations of the excitation pulse pair and the probe pulse. The signal has a sharp peak around zero which is followed by a prominent recurrence at ∼40 fs. Subsequently, the signal decays on an ∼200 fs time scale.

Although the 5-fs pulses have enough spectral bandwidth to excite more than one of the *p*-states at once, there is no indication of quantum beats that are associated with the presence of several vibronic transitions.[66] From the calculated splitting between the different *s*–*p* subbands[18,23,24] one expects the quantum beats with an ∼10-fs period. This raises the question about the exact meaning of the three *p*-states found in the quantum molecular dynamics simulations. The separate bands arise from the following procedure: in each snapshot corre-sponding to one time step in the simulation (1 fs), the three *p*-states were ordered by energy and the spectrum is subse-quently decomposed into contributions from each of the three transitions. This procedure does not incorporate the important factor of the time scale at which the energy of each of the *p*-states changes in time. As was shown above, the electronic dephasing for the *s*–*p* transition is exceptionally fast, giving rise to an extremely broad homogeneous absorption line-shape. This means that every *s*–*p* transition rapidly samples all possible energy differences within the absorption spectrum. Therefore, we cannot assign to the latter three separate bands with each of them corresponding to a separate *s*–*p* transition. As a matter of fact, the total spectrum consists of the sum of three bands
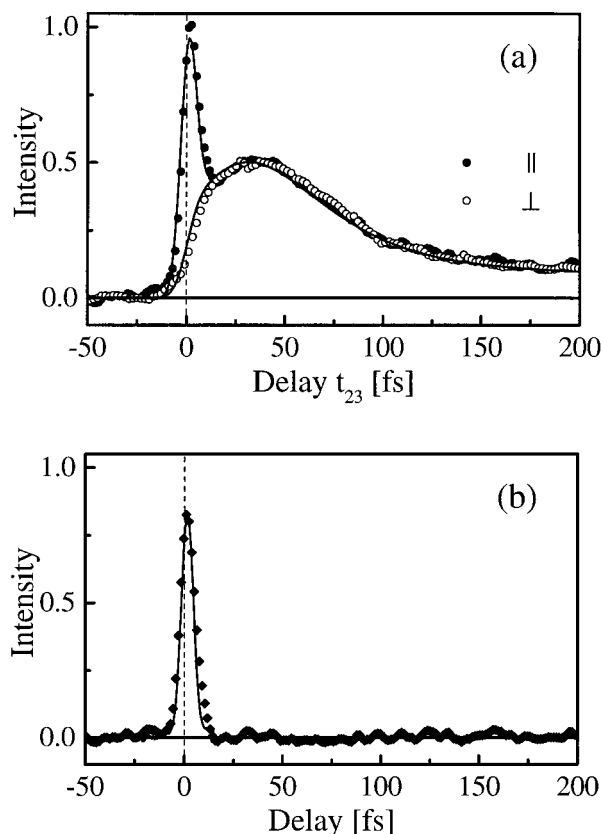

Figure 10. Transient grating signals obtained from the hydrated electron in H_2O (a) and their difference (b). Solid dots and open circles in (a) represent experimental data measured with the parallel and perpendicular polarization of excitation pulses, respectively. Solid curves in (a) depict the fits calculated as described in section 4.4. The signal difference is shown in (b) by filled diamonds while solid curve gives the two-pulse echo signal from Figure 8b for comparison. Note that the nonzero difference is confined in the region where the pulses overlap in time.

with approximately the same width as the total spectrum and nearly identical central frequencies. As a result, no quantum beats can be observed under these circumstances.

Next we focus on the origin of the narrow peak around zero and the subsequent recurrence in the TG signal. In the earlier papers on experiments with a 15-fs time resolution,[52,53] we suggested that a similar shape of TG transients was caused by librational motions of water molecules in the first solvation shell. Upon excitation a coherent wave packet is created that undergoes underdamped oscillatory motion on the excited-state potential surface. The return of the wave packet to the inner turning point gives rise to the recurrence in time-resolved optical signals. The signal amplitude near $t_{23} = 0$ is indeed higher than that of the recurrence due to two main reasons: the damping of the wave packet and additional coupling between interaction pulses near zero delay known as coherent artifact.[106,107] The latter is a manifestation of extra contributions to the TG signal originating from irregular time ordering of the excitation pulses. For example, around zero delays the second pulse E_2 is scattered from the grating imprinted by pulses E_1 and E_3, thus leading to the increased signal.

However, if the polarization of the excitation pulse pair and the probe pulse is orthogonal (Figure 10a, solid dots), the peak around zero vanishes. The second intriguing feature of the transient is that its amplitude is precisely equal to the one obtained with the collinear polarizations. This is highlighted in Figure 10b, where the difference between the two signals is
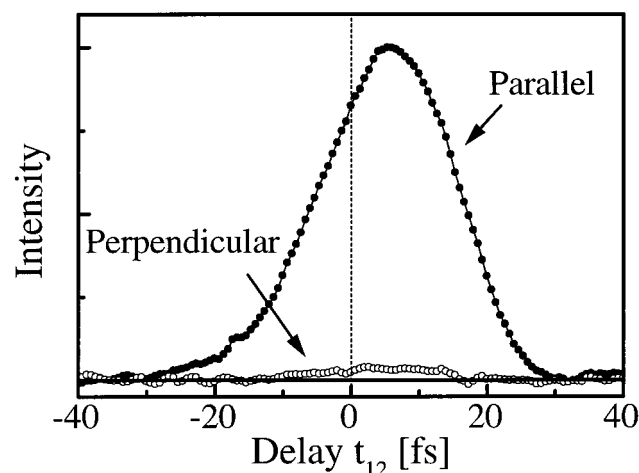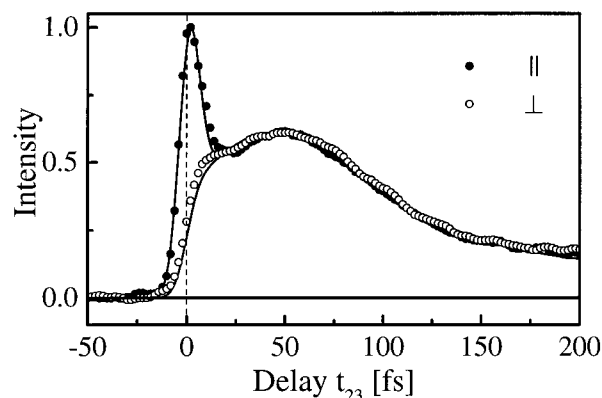
Figure 11. Two pulse photon echo signals from hydrated electrons in H_2O. Solid dots and open circles show the signals obtained, respectively, with parallel and perpendicular polarizations of the laser pulses. To ensure identical pulse intensities and focusing conditions, these measurements were performed with 15-fs laser pulses. Note that virtually no signal is detected in the case of perpendicular polarizations.

Figure 12. Transient grating signals obtained from the hydrated electron in D_2O. Solid dots and open circles show TG signals measured with the parallel and perpendicular polarization, respectively. Solid curves depict the fits calculated as described in section 4.4.

shown. For comparison, we also depicted the two-pulse photon echo signal from Figure 8b. Obviously, the nonzero part of the difference between the TG signals with parallel and orthogonal polarizations is confined to the region of the pulse overlap. Note that this is highly uncommon because usually the signal obtained with parallel polarizations is stronger than the one obtained with orthogonal polarizations because of polarization anisotropy.[108] That is, only after some time, that the amplitudes of the two signals become equal as a consequence of rotational diffusion processes which randomize the preferential orientation of dipole moments induced by the first pulse(s).

Clearly, the situation in the case of the hydrated electron is entirely different. As we have shown in section 4.1, the absorption spectrum of the hydrated electron is primarily homogeneously broadened. The underlying mechanism is that the charge distribution in the ground state rapidly samples many configurations with different orientations. The time scale at which the sampling takes place is shorter than the duration of 5-fs excitation pulses. The hydrated electron experiences a variety of possible orientations of the neighboring water molecules *during* the excitation process. Therefore, the orientations of the excited *p*-state are completely randomized by the time the excitation is completed. As a result, no anisotropy can be observed after the excitation pulse pair ends.

We conclude that, in the case of the aqueous electron, the transient anisotropy disappears in less than 5 fs. The important consequence is that when the polarizations of the pump pulses and the probe pulse are perpendicular, the coherent coupling between them is extremely ineffective. Therefore, if the contributions with irregular time ordering (as, for instance, E_1-E_3-E_2) are omitted, the total number of permutations is decreased by a factor of 2.[81] Hence, the TG signal near $t_{23} = 0$ for perpendicular polarizations is expected to be approximately one-fourth of the signal with parallel polarizations. This is value is very close to the one observed in the experiment (Figure 10a).

To verify this finding, we performed a two-photon echo spectroscopy with parallel and perpendicular polarizations of two pulses. In this experiment, the time ordering is essentially identical to the irregular time ordering around zero delay in the TG scan. The use of 15-fs pulses directly from the cavity-dumped laser allowed us to easily control the polarizations while maintaining constant energy of the pulses. For this purpose, a

zero-order $\lambda/2$ plate (Karl Lambrecht) was introduced in one of the spectrometer arms. Note that this is hardly possible in the case of 5-fs pulses since the $\lambda/2$ plate cannot equally rotate the polarization of spectral components in the 600−1100 nm range. The results of the experiments are presented in Figure 11. The signal in the case of perpendicular polarizations (solid circles) is suppressed by a factor of ∼30 compared to the signal with parallel polarizations (open circles). This proves our conclusion that the efficiency of the excitation of the hydrated electron with two pulses having orthogonal polarizations, is extremely low.

Based on the data obtained in polarization-dependent photon echo and TG spectroscopy, we reach a conclusion that the signal at short delays is substantially weaker than that at ∼40 fs. Therefore, there is no recurrence but rather a *delayed response* in the TG signal. The TG data for the orthogonal polarizations clearly indicate that the delayed response cannot be explained by underdamped wave packet dynamics. In that case, the signal would *always* be the largest at $t_{23} = 0$ due to inevitable damping of coherent motions.

The mechanism we suggest to explain the delayed response is that the transition dipole moment of the hydrated electron increases as a function of time after the initial excitation. Since the amplitude of the TG signal depends on the transition dipole moment (consult eqs 9 and 17), the signal increases before falling due to irreversible energy relaxation. The rise in the transition dipole moment should be directly connected to the strong coupling between the hydrated electron and water molecules that begin to readjust their positions after the excitation to minimize the total free energy of the system. The dependence of the transition dipole moment on nuclear degrees of freedom is known in molecular spectroscopy as the non-Condon effect.[109]

We next determine the microscopic motions of water molecules underlying the non-Condon effect. For this, we performed the TG experiment on the electron solvated in heavy water (Figure 12a). The TG signals are quite similar to those for normal water (Figure 10a), but the maximum is delayed to longer times (∼60 fs). However, if the time scale of the D_2O TG data is compressed by $\sqrt{2}$, the TG signal becomes virtually indistinguishable from that for H_2O (Figure 13). The difference in time scale can be explained by the fact that the moments of inertia of H_2O and D_2O differ precisely by a factor of 2. This immediately leads us to the conclusion that the maximum in the TG signals is caused by an *overdamped* librational motion of the water molecules. The specific dependence on deuteration

Photoexcited Hydrated Electron Dynamics

J. Phys. Chem. A, Vol. 103, No. 49, 1999 **10077**
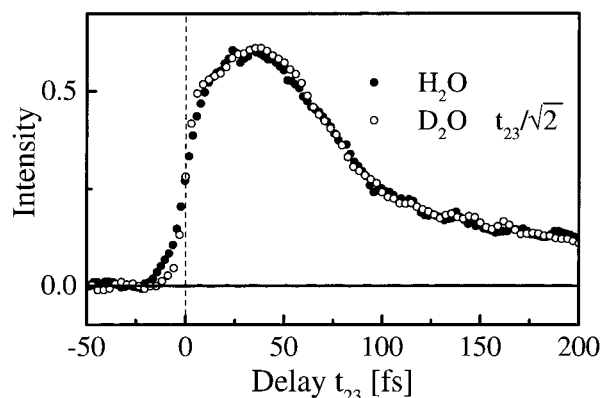
Figure 13. Comparison of the transient grating signals obtained from electrons hydrated in H_2O (solid dots) and D_2O (open circles). All data are given for perpendicular polarizations of excitation pulses. The delay-axis for D_2O has been compressed by a factor of $\sqrt{2}$ to highlight the isotopic effect.

rules out translations because the total mass of a water molecule changes only by a factor of 18/20. Another mechanism for the $\sqrt{2}$ dependence proposed by Barnett et al.[34] is free rotational diffusion of water molecules surrounding the electron. However, this explanation is not very likely. Rotations of molecules in a liquid can hardly be called free, especially in the case of a strongly hydrogen-bonding liquid like water. Furthermore, there is no signature of free rotations in the Raman spectrum of water.[110]

4.3. Early-Time Dynamics: The Microscopic Picture. The microscopic picture underlying the early-time dynamics of the hydrated electron that has emerged from our experiments is schematically presented in Figure 14. In this cartoon, only four of the approximately six water molecules in the first solvation shell around the electron are depicted for the sake of simplicity. The blue contour in the left panel shows the charge distribution (i.e., squared modulus of the wave function) of the hydrated electron. We assumed that the latter is confined in a harmonic potential formed by the neighboring water molecules (right panel). The use of, for example, square-shaped potential does not alter the main conclusions. The relevant mean size of the electron cloud in the ground $|g\rangle$ state was matched to value reported by the group of Rossky (1.9 Å),[24] while the distances between the electron and the water molecules were taken from ref 20.

Before excitation, the electron finds itself in the *s*-like ground state in equilibrium with surrounding water molecules (Figure 14a, left panel). Upon excitation, the electron makes a transition to the excited *p*-state wave function that is elongated in a particular direction (Figure 14b, left panel). Since the excitation pulses are very short, the water molecules have no time to react and, therefore, they still preserve their compact geometry. However, as time progresses, the water molecules in the first solvation shell are being pushed away by the expanded charge distribution of the electron (Figure 14c, left panel). We have already concluded from the TG experiments that the underlying microscopic processes at this stage are the librations of water molecules schematically shown by curved arrows in Figure 14c. This reorientational motion makes the potential energy well in which the electron is confined shallower as shown in Figure 14c, right panel. Subsequently, the charge distribution of the electron expands even further (Figure 14d), and so on.

Expansion of the cavity occupied by the electron has a profound effect on the wave function of the *unoccupied* ground-state as well. As the water molecules in the first solvation shell
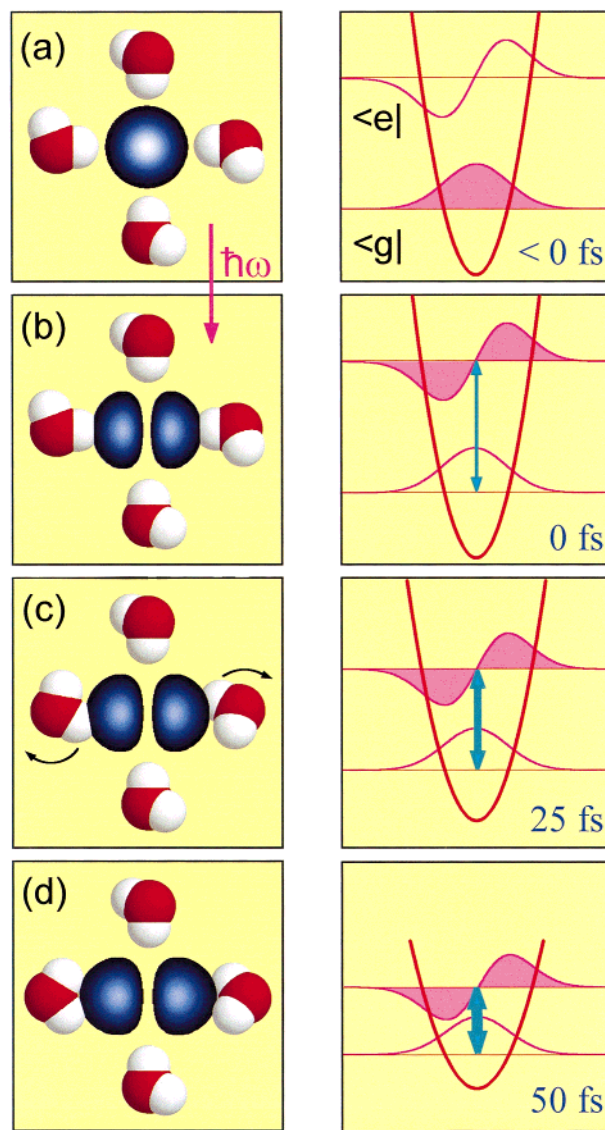
Figure 14. Artist's impression of the early-time dynamics of the hydrated electron. Left panel: configuration of the charge distribution of the electron (blue contour plot) and surrounding water molecules. Right panel: the potential-energy well in which the electron is confined (red curve) and the wave functions in the ground $<g|$ and excited $<e|$ states. The wave function of the currently occupied level is pink-shaded. The delay time after the initial excitation is shown in the right bottom corner of the right panel. The thickness of the arrow corresponds to the magnitude of the transition dipole moment.

are readjusting their orientations, the ground-state wave function is elongating in the same direction as the excited-state wave function (Figure 14, right panel). Therefore, the dipole moment of the electronic $p \rightarrow s$ transition, μ_{eg}, becomes larger due to the increased overlap between the probability densities of the ground and excited states. For instance, in the case of a harmonic potential the transition dipole moment increases inversely proportional to the square root of the oscillation frequency $\mu_{eg} \propto 1/\sqrt{\omega_0}$. The amplitude of the TG signal depends on the fourth power of the transition dipole moment that changes in time. Hence a very moderate extension of the electron cloud leads to a substantial increase of the TG signal, as was observed experimentally (Figure 10 and 12).

The position of the maximum in the TG signal gives us an estimate for the time scale of the expansion of the first solvation shell: ~50 fs. The frequencies that correspond to this time
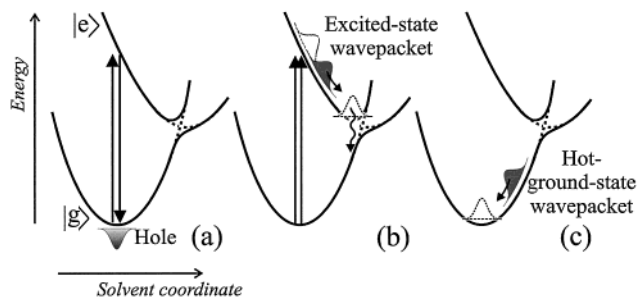
Figure 15. Schematic representation of the wave packet dynamics on the ground- and excited-state potentials. (a) Ground-state bleaching. (b) Excited-state wave packet movement, corresponding to the red-shifting in time of the stimulated emission spectrum. (c) Wave packet propagation on the hot ground state, causing the blue shifting in time of the induced absorption spectrum. Solid vertical arrows indicate the excitation process.

coincide reasonably well with librational band of water which spans the range $\sim 300-900$ cm^{-1}, and which also scales with $\sqrt{2}$ upon deuteration.[110] The decay following the maximum in the signal is most probably caused by relaxation down to the ground state at the 125-fs time scale.[33] The stimulated emission is rapidly diminished due to the decreasing population on the excited state, while at the same time the equlibrating ground state gives rise to induced absorption.

4.4. Theoretical Model. To put the microscopic picture of the solvation of the hydrated electron developed in the previous section on a more quantitative ground, we next introduce a simple model based on wave packet dynamics on the ground and the excited states (Figure 15). In this picture, we assume that prior to the photoexcitation the ground state of the hydrated electron is equilibrated. The excitation pulse pair creates a hole in the ground state distribution (Figure 15a) and a wave packet in the excited state (Figure 15b). This gives rise to a bleach of the ground-state absorption and to a stimulated emission from the excited state. Assuming that no population relaxation takes place yet on the duration of the applied laser pulses and the optical transition is primarily homogeneously broadened, both the bleach and the stimulated emission contours have approximately the same spectral shape as the steady-state absorption band.

Immediately after the excitation, the contours of the bleach and the stimulated emission are exactly identical. Subsequently, the downhill movement of the wave packet on the excited state potential takes place, which reflects the gradual expansion of the water cavity. Because the energy gap between the two potentials decreases as the wave packet moves on the excited state surface, the stimulated emission band becomes increasingly red-shifted with respect to the ground-state bleach whose spectral position remains fixed (Figure 15a,b).

The expression for the observed TG signal can be easily calculated in the slow diffusion limit.[66,111] Based on the finding of predominantly homogeneous dephasing in section 4.1, we assume the nonlinear response function of the ground state, $R_{gr}(t_1,t_2,t_3)$, in the form given by eq 15. The nonlinear response function associated with the populated excited state is then given by[111]

$$R_{ex}(t_1,t_2,t_3) = R_{gr}(t_1,t_2,t_3) \exp\{i\Delta\omega t_3[1 - M(t_{23})]\} \quad (23)$$

where $\Delta\omega$ is the Stokes shift, i.e., the spectral shift of absorption (fluorescence) due to energy reorganization, and $M(t)$ is the electronic band gap correlation function.[66] Here we assumed that $M(t)$ changes slowly on the time of electronic dephasing,

characterized by T_2. Adapting the model of an overdamped vibration,[66] $M(t)$ then can be expressed as

$$M(t) = \exp\left(-\frac{t}{t_{ex}}\right) \qquad t_{ex} \gg T_2 \quad (24)$$

To obtain the spectral shape of the ground- and excited-state contributions we now Fourier transform $R_{gr}(t_1,t_2,t_3)$ and $R_{ex}(t_1,t_2,t_3)$. The resulting third-order susceptibility for the ground-state contribution to the nonlinear signal is given by eq 17 while the $\tilde{\chi}^{(3)}$ contribution of the populated excited state is expressed by

$$\tilde{\chi}_{ex}^{(3)}(t_{23},\omega_{eg}-\omega',\omega'-\omega'',-\omega_{eg}+\Omega) = -i\frac{\mu_{eg}^4 N}{\hbar^4} \times$$

$$\frac{1}{T_1^{-1}-i(\omega''-\omega')}\left[\frac{1}{T_2^{-1}-i(\omega_{eg}-\omega')} + \frac{1}{T_2^{-1}-i(\omega''-\omega_{eg})}\right] \times$$

$$\frac{1}{T_2^{-1}+i\left(\omega_{eg}-\Delta\omega\left[1 - \exp\left(-\frac{t_{23}}{t_{ex}}\right)\right] - \Omega\right)} \quad (25)$$

Analogous to the wave packet in the excited state, one can include into consideration the wave packet sliding down the (hot) ground state.

As described in the previous section, the expansion of the solvent cavity forced by the photoexcitation leads to the increase of the transient dipole moment magnitude as a function of time, which gives rise to the non-Condon effect. Therefore, it is assumed that the change of the transition dipole moment strength occurs on the same time scale as the motion of the excited-state wave packet. This change does not influence the magnitude of the absorption bleach band since the latter is caused by a static hole in the ground state. On the other hand, the magnitude of the spectral contribution, caused by the traveling wave packets, is dependent on the changing strength of the transition dipole moment. Therefore, μ_{eg} in eq 25 should be considered as a function of time, i.e.,

$$\mu_{eg}(t) = \mu^0 F_{NC}(t) \quad (26)$$

where μ^0 is the initial dipole moment and the non-Condon parameter, $F_{NC}(t)$, is a slowly changing function compared with the pulse duration.

After about 200 fs, the excited-state wave packet reaches the region where the potentials of the ground and the excited states cross.[33] In this region, the wave packet "leaks" from one potential surface to another. However, the crossing occurs to a modified (hot) ground state that has to "cool" before reaching the equilibrated steady state. Therefore, the hot ground state wave packet gives rise to an induced absorption band that shifts from the red to the blue and eventually cancels the ground-state bleach (Figure 15c). In the model, this crossing process is taken into account by assuming that the excited-state stimulated emission vanishes at the same rate as the hot ground-state absorption builds up.

We next calculate the TG signal according to the formalism developed in section 2.1. If the population relaxation time T_1 is long compared to the pulse duration, in eq 17 and eq 25 one can assume $\tilde{\chi}^{(3)} \propto \delta(\omega'-\omega'')$. Then, integrating eq 9 over frequency Ω and making use of eqs 7, 17, and 25, and accounting for the hot-ground-state contribution, we arrive at

Photoexcited Hydrated Electron Dynamics

J. Phys. Chem. A, Vol. 103, No. 49, 1999 **10079**

$$S_{TG}(t_{12} = 0, t_{23}) \propto |\mu^0|^8 \int I(\Omega)|\sigma_{gr}(\Omega) + \sigma_{ex}(\Omega) -$$
$$\sigma_{hot-gr}(\Omega)|^2 \, d\Omega \quad (27)$$

Here, $I(\Omega)$ is the spectrum of excitation pulses and the contributions from the ground, excited, and hot ground state potentials are respectively written as

$$\sigma_{gr}(\Omega) = \sigma_A(\Omega) \quad (28)$$

$$\sigma_{ex}(\Omega) = F_{NC}^4(t_{23}) \exp(-\gamma_c t_{23})\sigma_A(\Omega +$$
$$\Delta\omega[1 - \exp(-\gamma_{ex}t_{23})]) \quad (29)$$

$$\sigma_{hot-gr}(\Omega) = F_{NC}^4(t_{23})[1 -$$
$$\exp(-\gamma_c t_{23})]\sigma_A(\Omega + \Delta\omega \exp(-\gamma_{gr}t_{23})) \quad (30)$$

where $\sigma_A(\Omega)$ is the steady-state absorption spectrum, $\Delta\omega$ is the Stokes shift, γ_{ex} and γ_{gr} are the rates at which the wave packet moves on the excited and the ground states, respectively, and γ_c is the crossing rate from the excited state to the ground state.

The expressions given by eq 28−30 represent Lorentzian line shapes described by eq 22. These constituent terms of the TG signal are schematically depicted in Figure 15a−c in their respective order. The first term is static and stands for the hole in the ground state (Figure 15a). The second and the third ones account for the moving wave packet in the excited (Figure 15b) and hot ground (Figure 15c) states, respectively. The use of RWA[65,66] in derivation of eqs 17 and 25 leads to symmetric Lorentzian contours, rather than the asymmetric extended line-shape given by eq 21 employed to explain the absorption spectrum in section 4.1. The spectrally integrated TG signal, however, is insensitive to such a minute difference in the spectral contours, which justifies the use of centrosymmetric line-shape in our calculations.

The physical meaning of the movement of the Lorentzian wave packet can be explained as follows: The difference in *curvature* of the ground and excited-state potentials implies a strong quadratic electron vibration coupling that is responsible for the extraordinary amount of homogeneous *spectral broadening*. On the other hand, linear electron vibration coupling determines, at large, the presence of the *wave packet dynamics*. This is due to predominantly linear change of the energy gap with the nuclear coordinate between the ground and excited states as a result of the *displacement* of their potentials with respect to each other.

The time-dependent non-Condon parameter is assumed to be equal to

$$F_{NC}(t_{23}) = 1 + f_{NC}[1 - \exp(-\gamma_{ex}t_{23})] \quad (31)$$

where f_{NC} is a measure of the strength of the non-Condon effect or, in other words, the ratio of the magnitudes of the initial and maximal dipole moments. The influence of the non-Condon effect on the TG signal is illustrated in Figure 16. With a constant transition dipole moment ($f_{NC} = 0$), the TG signal peaks close to zero (Figure 16a). If the non-Condon strength is chosen to be 0.5, the dipole moment grows as a function of time, and reaches a maximum after ~100 fs (Figure 16b). Subsequently, it balances the drop in the TG signal due to population relaxation, which results in a maximum that is significantly shifted away from zero (Figure 16c).

To incorporate the fact that we are dealing with the pulses of finite duration, we convoluted the signal given by eq 27 with
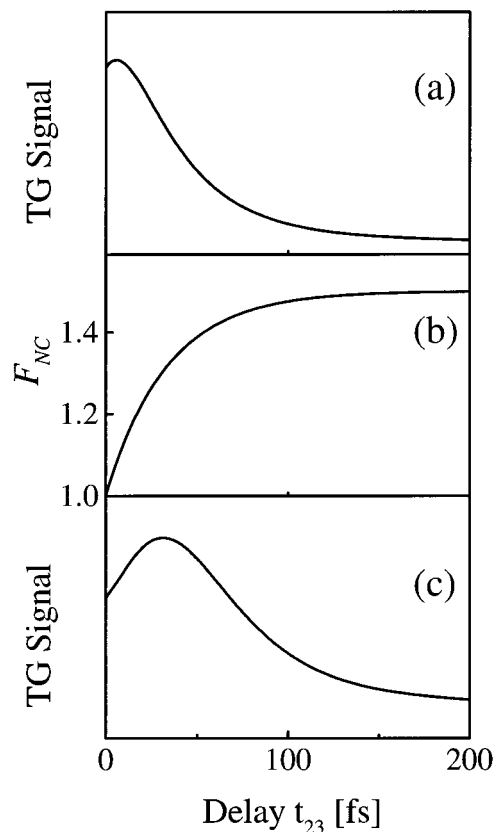
Figure 16. Simulated transient grating signals for perpendicular polarization of excitation pulses. (a) Signal without non-Condon effect ($f_{NC} = 0$). (b) Transition dipole moment as a function of time with a non-Condon effect present. (c) The transient grating signal from (a) when the non-Condon effect is taken into account.

the instrument response. The following parameters are taken for water: $1/\gamma_{ex} = 33$ fs; $1/\gamma_{gr} = 300$ fs; $1/\gamma_c = 125$ fs; $\Delta\omega = 0.50$ PHz; $f_{NC} = 0.5$. For heavy water, all rates are decreased by a factor $\sqrt{2}$ in accordance with the established fact that underlying microscopic dynamics are determined by librations. The calculated TG signals for H_2O and D_2O are depicted in Figures 10a and 12, respectively. Evidently, by inclusion of the non-Condon effect we are well able to reproduce the delayed maximum in the TG signals, even though the rate of increase of the transition dipole moment is not an independent variable. As can be seen from eqs 29 and 31, we ascribed a single common rate, γ_{ex}, to the evolution of both the transition dipole moment strength and the dynamic Stokes shift. The fact that we can fit the experimentally observed dependencies reflects the common microscopic origin of the dynamic Stokes shift and the non-Condon effect: the unidirectional expansion of the solvent cavity caused by librational reorientation of the water molecules.

We predict that the time constant of populating the hot ground state is ~125 fs for H_2O. Careful inspection of the measured TG traces (Figure 10a) shows that at this point there is a slight bend in the curvature. Apparently, this is a signature of the interplay between stimulated emission from the excited state that is being diminished and the induced hot ground-state absorption that is being increased simultaneously. After this, the induced ground-state absorption shift to the blue on a time scale of 300 fs. This shows up as the slower decay in the transient grating.

5. Conclusions

Photon echo and transient grating spectroscopy on the hydrated electron performed with the best time resolution available to date has provided a powerful insight in the microscopic processes that underlie solvation dynamics.

To solve the nontrivial fundamental issues related to nonlinear spectroscopy with optical pulses that consist of 2.5 optical cycles, we developed a general formalism describing the generated signal field in both the time and frequency domains. The frequency domain representation is found to be more powerful since it allows a consistent account of a variety of effects, such as phase mismatch, self-steepening, dispersive pulse broadening, etc. Additionally, the use of the frequency domain formalism removed the necessity to invoke a number of approximations such as, for example, the slowly varying envelope approximation. The derived formulation also avoids the use of parameters that are ill-defined for broadband optical pulses such as, for instance, the carrier frequency of the pulse. Equations 7−10 constitute the backbone of the general description of a third-order nonlinear experiment. Importantly, these equations remain valid and could be directly applied even for single-cycle pulses.

We have developed a general procedure for calculating the spectral filter effect. Such a routine should be employed to optimize the experimental configuration for any third-order spectroscopic experiment that utilizes laser pulses shorter than 10 fs. In particular, one can design a compensating filter to account for spectral filtering effects and place it in front of the light detector. Notably, a careful choice of the beam geometry and selection of a photodetector with the suitable spectral sensitivity, as has been done in our experiments, can illuminate the need for a separate compensating filter. We next have demonstrated that the ability to defeat the damaging role of the spectral filter effect legitimizes a transition to the typically employed for the multicycle pulse time domain formulation. Importantly, for the weak signal applications, the absence of spectral filtering eliminates the otherwise unavoidable requirement to frequency resolve the signals.

Both two-pulse photon echo and TG experiments, involving two and three femtosecond pulses, respectively, have been performed on equilibrated hydrated electrons. By comparing two-pulse echo signals from hydrated electrons and from water alone, we have derived the pure dephasing time of ∼1.6 fs. We have shown that the absorption band of equilibrated solvated electrons in water is predominantly homogeneously broadened and succeeded in modeling the whole absorption spectrum of the hydrated electrons by a single homogeneous line shape. The typically employed symmetric Lorentzian line shape has been abandoned in favor of a more general expression for a homogeneously broadened line. Importantly, in the line shape used in our fit, the long-puzzling issue of the asymmetry of the absorption spectrum found a natural explanation. Further proof of the homogeneous nature of the absorption spectrum comes from the absence of quantum beats on the 10-fs time scale in the TG signal, pointing to the fact that the absorption spectrum does not consist of three separate absorption bands.

The TG experiments on the hydrated electron with perpendicular polarziations of excitation pulses have revealed a delayed response never observed before due to limited time resolution. We have suggested that the delayed response is due to a non-Condon effect, caused by librational motions of the water molecules surrounding the electron. The large magnitude of the non-Condon effect is a direct consequence of the fact that the Hamiltonian of the hydrated electron is fully determined by the configuration of the neighboring water molecules. This renders the hydrated electron a convenient probe for the local structure of water, the most-important-for-life but still mysterious liquid.[21] We have also shown that a numerical model including the non-Condon effect due to initial librational motion of water molecules, and subsequent population relaxation and ground-state cooling can reproduce the essential features of the observed signals, putting our ideas on solid ground.

Electron in polar liquids continues to be a vast experimental and theoretical field in which many intriguing questions remain to be answered. There are still many conflicting and not well understood issues concerning electron equilibration,[49,112] energy relaxation of the photoexcited electrons in fluids,[33,55] the nature and the number of the bound localized and unbound states of the electron trapped in the solvent cavity,[23,46] etc. In the current paper we have addressed only the earliest part of the energy dissipation that directly follows photoexcitation. The subsequent relaxation processes, albeit taking place on a slower time scale, are no less interesting or less controversial. In particular, the questions about the lifetime of the bound excited state and the involvement of the quasi-continuum states, predicted by quantum molecular dynamics simulations,[24] have to be addressed.

New, emerging spectroscopic techniques could help clarify many mysteries of this attractive and challenging system. We foresee great prospects for the application of the femtosecond infrared spectroscopy.[113] By temporally and spectrally resolving of the transient dynamics of the OH bond that has infrared absorption, one would obtain an invaluable direct insight into the motions of the solvent molecules as to how they respond to the photoexcitation of the solvated electron. Another promising technique that has been gaining its strength in the last years due to the enormous progress in femtosecond technology is combined femtosecond visible X-ray spectroscopy.[114−116] Recent experiments on GaAs lattice dynamics studied by picosecond X-ray diffraction[117] clearly demonstrated the feasibility of this approach toward physical and chemical processes.

References and Notes

(1) Weyl, W. *Pogg. Ann.* **1864**, *123*, 350.
(2) Kraus, C. A. *J. Am. Chem. Soc.* **1908**, *30*, 1323−1344.
(3) Hart, E. J.; Boag, J. W. *J. Am. Chem. Soc.* **1962**, *84*, 4090.
(4) Boag, J. W.; Hart, E. J. *Nature* **1963**, *197*, 45.
(5) Borja, M.; Dutta, P. K. *Nature* **1993**, *362*, 43−44.
(6) Sykora, M.; Kincaid, J. R. *Nature* **1997**, *387*, 162−163.
(7) Bach, U.; Lupo, D.; Comte, P.; Moser, J. E.; Weissörtel, F.; Salbeck, J.; Spreitzer, H.; Grätzel, M. *Nature* **1998**, *395*, 583−584.
(8) Khaselev, O.; Turner, J. A. *Science* **1998**, *280*, 425−426.
(9) Stowell, M. H. B.; McPhillips, T. M.; Rees, D. C.; Soltis, S. M.; Abresch, E.; Feher, G. *Science* **1997**, *276*, 812−816.

Photoexcited Hydrated Electron Dynamics

J. Phys. Chem. A, Vol. 103, No. 49, 1999 **10081**

(10) Steinberg-Yfrach, G.; Liddell, P. A.; Hung, S.-C.; Moore, A. L.; Gust, D.; Moore, T. A. *Nature* **1997**, *385*, 239−240.

(11) Schindelin, H.; Kisker, C.; Schlessman, J. L.; Howard, J. B.; Rees, D. C. *Nature* **1997**, *387*, 370−376.

(12) Alivisatos, A. P. *Science* **1996**, *271*, 933−936.

(13) Kouwenhoven, L. P.; Oosterkamp, T. H.; Danoesastro, M. W. S.; Eto, M.; Austing, D. G.; Honda, T.; Tarucha, S. *Science* **1997**, *278*, 1788−1791.

(14) McEuen, P. L. *Science* **1997**, *278*, 1729.

(15) Stewart, D. R.; Sprinzak, D.; Marcus, C. M.; Duruöz, C. I.; Harris, J. S., Jr. *Science* **1997**, *278*, 1784−1787.

(16) Oosterkamp, T. H.; Fujisawa, T.; Wiel, W. G. v. d.; Ishibiashi, K.; Hijman, R. V.; Tarucha, S.; Kouwenhoven, L. P. *Nature* **1998**, *395*, 873−876.

(17) Hasen, J.; Pfeiffer, L. N.; Pinczuk, A.; He, S.; West, K. W.; Dennis, B. S. *Nature* **1997**, *390*, 54−56.

(18) Schwartz, B. J.; Rossky, P. J. *J. Chem. Phys.* **1994**, *101*, 6902−6916.

(19) Park, I.; Cho, K.; Lee, S.; Kim, K.; Joannopoulos, J. D., to be published.

(20) Kevan, L. *Acc. Chem. Res.* **1981**, *14*, 138.

(21) Mishima, O.; Stanley, H. E. *Nature* **1998**, *396*, 329−335.

(22) Romero, C.; Jonah, C. D. *J. Chem. Phys.* **1988**, *90*, 1877−1887.

(23) Rossky, P. J.; Schnitker, J. *J. Phys. Chem.* **1988**, *92*, 4277−4285.

(24) Schnitker, J.; Motakabbir, K.; Rossky, P. J.; Friesner, R. *Phys. Rev. Lett.* **1988**, *60*, 456.

(25) Staib, A.; Borgis, D. *J. Chem. Phys.* **1995**, *103*, 2642.

(26) Kajiwara, T.; Funabashi, K.; Naleway, C. *Phys. Rev. A* **1972**, *6*, 808−816.

(27) *Electron solvent and anion solvent interactions*; Kevan, L., Webster, B. C., Eds.; Elsevier: Amsterdam, 1976.

(28) Banerjee, A.; Simons, J. *J. Chem. Phys.* **1978**, *68*, 415−432.

(29) Carmichael, I. *J. Phys. Chem.* **1980**, *84*, 1076−1082.

(30) Bartczak, W. M.; Hilczer, M.; Kroh, J. *J. Phys. Chem.* **1987**, *91*, 3834−40.

(31) Lugo, R.; Delahay, P. *J. Chem. Phys.* **1972**, *57*, 2122−2129.

(32) Jou, F.-Y.; Freeman, G. R. *J. Phys. Chem.* **1979**, *83*, 2383.

(33) Assel, M.; Laenen, R.; Laubereau, A. *J. Phys. Chem. A* **1998**, *102*, 2256−2262.

(34) Barnett, R. B.; Landman, U.; Nitzan, A. *J. Chem. Phys.* **1989**, *90*, 4413.

(35) Schwartz, B. J.; Rossky, P. J. *J. Chem. Phys.* **1994**, *101*, 6917−6926.

(36) Schwartz, B. J.; Rossky, P. J. *J. Phys. Chem.* **1995**, *99*, 2953−2958.

(37) Schwartz, B. J.; Rossky, P. J. *J. Mol. Liq.* **1995**, *65/66*, 23−30.

(38) Graf, P.; Nitzan, A.; Diercksen, G. H. F. *J. Phys. Chem.* **1996**, *100*, 18916−18923.

(39) Schwartz, B. J.; Bittner, E. R.; Prezhdo, O. V.; Rossky, P. J. *J. Chem. Phys.* **1996**, *104*, 5942−5955.

(40) Schwartz, B. J.; Rossky, P. J. *J. Chem. Phys.* **1996**, *105*, 6997−7010.

(41) Berg, M. A. *J. Chem. Phys.* **1999**, *110*, 8577−8588.

(42) Migus, A.; Gauduel, Y.; Martin, J. L.; Antonetti, A. *Phys. Rev. Lett.* **1987**, *58*, 1559−62.

(43) Long, F. H.; Lu, H.; Eisenthal, K. B. *Phys. Rev. Lett.* **1990**, *64*, 1469−72.

(44) Messmer, M. C.; Simon, J. D. *J. Phys. Chem.* **1990**, *94*, 1220−1223.

(45) Alfano, J. C.; Walhout, P. K.; Kimura, Y.; Barbara, P. F. *J. Chem. Phys.* **1993**, *98*, 5996−5998.

(46) Kimura, Y.; Alfano, J. C.; Walhout, P. K.; Barbara, P. F. *J. Phys. Chem.* **1994**, *98*, 3450−3458.

(47) Reuther, A.; Laubereau, A.; Nikogosyan, D. N. *J. Phys. Chem.* **1996**, *100*, 16794−16800.

(48) Shi, X.; Long, F. H.; Lou, H.; Eisenthal, K. B. *J. Phys. Chem.* **1996**, *100*, 11903−11906.

(49) Pépin, C.; Goulet, T.; Houde, D.; Jay-Gerin, J.-P. *J. Phys. Chem. A* **1997**, *101*, 4351−4360.

(50) Hertwig, A.; Hippler, H.; Unterreiner, A. N.; Vöhringer, P. *Ber. Bunsen-Ges. Phys. Chem., Chem. Phys.* **1998**, *102*, 805−810.

(51) Reid, P. J.; Silva, C.; Walhout, P. K.; Barbara, P. F. *Chem. Phys. Lett.* **1994**, *228*, 658−664.

(52) Emde, M. F.; Baltuska, A.; Kummrow, A.; Pshenichnikov, M. S.; Wiersma, D. A. *Phys. Rev. Lett.* **1998**, *80*, 4645−4648.

(53) Kummrow, A.; Emde, M. F.; Baltuška, A.; Pshenichnikov, M. S.; Wiersma, D. A. *J. Phys. Chem.* **1998**, *102*, 4172−4176.

(54) Silva, C.; Walhout, P. K.; Yokoyama, K.; Barbara, P. F. *Phys. Rev. Lett.* **1998**, *80*, 1086−1089.

(55) Yokoyama, K.; Silva, C.; Son, D. H.; Walhout, P. K.; Barbara, P. F. *J. Phys. Chem.* **1998**, *102*, 6957−6966.

(56) Baltuška, A.; Wei, Z.; Pshenichnikov, M. S.; Wiersma, D. A. *Opt. Lett.* **1997**, *22*, 102−104.

(57) Baltuška, A.; Wei, Z.; Szipöcs, R.; Pshenichnikov, M. S.; Wiersma, D. A. *Appl. Phys. B* **1997**, *65*, 175−188.

(58) Nisoli, M.; Silvestri, S. D.; Szipöcs, R.; Ferencz, K.; Spielmann, C.; Sartania, S.; Krausz, F. *Opt. Lett.* **1997**, *22*, 522−524.

(59) Nisoli, M.; Stagira, S.; Silvestri, S. D.; Svelto, O.; Sartania, S.; Cheng, Z.; Lenzner, M.; Spielmann, C.; Krausz, F. *Appl. Phys. B* **1997**, *65*, 189.

(60) Shirakawa, A.; Sakane, I.; Kobayashi, T. *Sub-5-fs pulse generation by pulse-fron-matched optical parametric amplification*; XIth International Conference on Ultrafast Phenomena, 1998, Garmisch-Parenkirchen, Germany, July 12−17, 1998.

(61) Allen, L.; Eberly, J. H. *Optical resonance and two-level atoms*; Dover Publications, Inc: New York, 1987.

(62) Butcher, P. N.; Cotter, D. *The elements of nonlinear optics*; Cambridge University Press: Cambridge, 1990.

(63) Shimoda, K. *Introduction to laser physics*, 2nd ed.; Springer-Verlag: Berlin, 1991.

(64) Brabec, T.; Krausz, F. *Phys. Rev. Lett.* **1997**, *78*, 3282−3285.

(65) Boyd, R. W. *Nonlinear optics*; Academic Press: San Diego, 1992.

(66) Mukamel, S. *Principles of Nonlinear Optical Spectroscopy*; Oxford University Press: New York, 1995.

(67) Weiner, A. M. *IEEE J. Quantum Electron.* **1983**, *QE−19*, 1276−1283.

(68) Taft, G.; Rundquist, A.; Murnane, M. M.; Christov, I. P.; Kapteyn, H. C.; DeLong, K. W.; Fittinghoff, D. F.; Krumbuguel, M. A.; Sweetser, J. N.; Trebino, R. *IEEE J. Select. Top. Quantum Electron.* **1996**, *2*, 575−585.

(69) Baltuška, A.; Pshenichnikov, M. S.; Wiersma, D. A. *IEEE J. Quantum Electron.* **1999**, *35*, 459−478.

(70) Pshenichnikov, M. S.; Baltuška, A.; Szipocs, R.; Wiersma, D. A. Sub-5-fs pulses: generation, characterisation, and experiments. In *Ultrafast Phenomena XI*; Elsaesser, T., Fujimoto, J. G., Wiersma, D. A., Zinth, W., Eds.; Springer: Berlin, 1998.

(71) Shen, Y. R. *The principles of nonlinear optics*; Wiley: New York, 1984.

(72) Schubert, M.; Wilhelmi, B. *Nonlinear optics and quantum electronics*; John Wiley: New York, 1986.

(73) Akhmanov, S. A.; Vysloukh, V. A.; Chirkin, A. S. *Optics of femtosecond laser pulses*; American Institute of Physics: New York, 1992.

(74) Agrawal, G. P. *Nonlinear fiber optics*, 2nd ed.; Academic Press: San Diego, 1995.

(75) Trebino, R.; DeLong, K. W.; Fittinghoff, D. N.; Sweetser, J.; Krumbügel, M. A.; Richman, B.; Kane, D. J. *Rev. Sci. Instrum.* **1997**, *68*, 3277−3295.

(76) *Release on the Refractive Index of Ordinary Water Substance as a Function of Wavelength, Temperature and Pressure*; The International Association for the Properties of Water and Steam: Erlangen, Germany, 1997.

(77) Harvey, A. H.; Gallagher, J. S.; Sengers, J. M. L. *J. Phys. Chem. Ref. Data* **1998**, *27*, 761−774.

(78) Bracewell, R. N. *The Fourier Transform and Its Applications*, 2nd ed.; McGraw-Hill: New York, 1986.

(79) Bloembergen, N. *Nonlinear Optics*; Benjamin: New York, 1965.

(80) Fleming, G. R. *Chemical Applications of Ultrafast Spectroscopy*; Oxford University Press: New York, 1986.

(81) de Boeij, W. P.; Pshenichnikov, M. S.; Wiersma, D. A. *J. Phys. Chem.* **1996**, *100*, 11806−11823.

(82) Matheson, M. S.; Mulac, W. A.; Rabani, J. *J. Phys. Chem.* **1963**, *67*, 2613−2617.

(83) Waltz, W. L.; Adamson, A. W. *J. Phys. Chem.* **1969**, *73*, 4250−4255.

(84) Shirom, M.; Siderer, Y. *J. Chem. Phys.* **1972**, *57*, 1013−1015.

(85) Lachish, U.; Shafferman, A.; Stein, G. *J. Chem. Phys.* **1975**, *64*, 4205−4211.

(86) Shirom, M.; Stein, G. *J. Chem. Phys.* **1971**, *55*, 3372−3378.

(87) Pommeret, S.; Naskrecki, R.; van der Meulen, P.; Menard, M.; Vigneron, G.; Gustavsson, T. *Chem. Phys. Lett.* **1998**, *288*, 833−840.

(88) Shirom, M.; Stein, G. *J. Chem. Phys.* **1971**, *55*, 3379−3382.

(89) Wiesenfeld, J. M.; Ippen, E. P. *Chem. Phys. Lett.* **1980**, *73*, 47−50.

(90) McMorrow, D.; Lotshaw, W. T.; Kenney-Wallace, G. A. *IEEE J. Quantum Electron.* **1988**, *24*, 443−454.

(91) McMorrow, D.; Lotshaw, W. T. *Chem. Phys. Lett.* **1990**, *174*, 85−94.

(92) McMorrow, D. *Opt. Commun.* **1991**, *86*, 236−244.

(93) Castner, E. W.; Chang, Y. J.; Chu, Y. C.; Walrafen, G. E. *J. Chem. Phys.* **1994**, *102*, 653−659.

(94) Palese, S.; Schilling, L.; Miller, R. J. D.; Staver, P. R.; Lotshaw, W. T. *J. Phys. Chem.* **1994**, *98*, 6308−6316.

(95) Neria, E.; Nitzan, A. *J. Chem. Phys.* **1993**, *99*, 515.

(96) Prezhdo, O. V.; Rossky, P. J. *Phys. Rev. Lett.* **1998**, *81*, 5294−5297.

(97) Siegman, A. E. *Lasers*; University Science Books: Mill Valley, California, 1986.

(98) Huppert, D.; Avouris, P.; Rentzepis, P. M. *J. Phys. Chem.* **1978**, *82*, 2282−2286.

(99) Baltuška, A.; Pshenichnikov, M. S.; Wiersma, D. A. manuscript in preparation.

(100) Aihara, M. *Phys. Rev. B* **1982**, *25*, 53−60.

(101) Grishanin, B. A.; Petnikova, V. M.; Shuvalov, V. V. *J. Appl. Spectrosc.* **1987**, *47*, 1278−1282.

(102) Grishanin, B. A.; Petnikova, V. M.; Shuvalov, V. V. *J. Appl. Spectrosc.* **1987**, *47*, 1309−1314.

(103) Toutounji, M.; Small, G. J.; Mukamel, S. *J. Chem. Phys.* **1998**, *109*, 7949−7960.

(104) Toutounji, M.; Small, G. J.; Mukamel, S. *J. Chem. Phys.* **1999**, *110*, 1017−1024.

(105) Osad'ko, I. S.; Stashek, M. V.; Mikhailov, M. A. *Laser Phys.* **1996**, *6*, 175−178.

(106) Pollard, W. T.; Matthies, R. A. *Annu. Rev. Phys. Chem.* **1992**, *43*, 497.

(107) Chachisvilis, M.; Fidder, H.; Sundström, V. *Chem. Phys. Lett.* **1995**, *234*, 141−150.

(108) Albrecht, A. C. In *Progress in reaction kinetics*; Porter, G., Ed.; Pergamon Press: Oxford, 1970; Vol. 5, p 301.

(109) Herzberg, G. *Spectra of Diatomic Molecules*, 2nd ed.; Van Nostrand: New York, 1950.

(110) De Santis, A.; Frattini, R.; Sampoli, M.; Mazzacurati, V.; Nardone, M.; Ricci, M. A.; Ruocco, G. *Mol. Phys.* **1987**, *61*, 1199.

(111) de Boeij, W. P.; Pshenichnikov, A. S.; Wiersma, D. A. *Chem. Phys.* **1998**, *233*, 287−309.

(112) Turi, L.; Holpar, P.; Keszei, E. *J. Phys. Chem.* **1997**, *101*, 5469−5476.

(113) Chudoba, C.; Nibbering, E. T. J.; Elsaesser, T. *Phys. Rev. Lett.* **1998**, *81*, 3010−3013.

(114) Raksi, F.; Wilson, K. *J. Chem. Phys.* **1996**, *104*, 6066.

(115) Ben-Nun, M.; Cao, J.; Wilson, K. R. *J. Phys. Chem. A* **1997**, *101*, 8743.

(116) Cao, J.; Wilson, K. R. *J. Phys. Chem. A* **1998**, *102*, 9523.

(117) Rose-Petruck, C.; Jimenez, R.; Guo, T.; Cavalleri, A.; Siders, C. W.; Raksi, F.; Squier, J. A.; Walker, B. C.; Wilson, K. R.; Barty, C. P. J. *Nature* **1999**, *398*, 310.